



AFRL-RY-WP-TR-2017-0199

CHIP-SCALE COMBINATORIAL ATOMIC NAVIGATOR (C-SCAN)

Low Drift Nuclear Spin Gyroscope

Michael Romalis

Princeton University

Thomas Kornack

Twinleaf, LLC

JANUARY 2018

Final Report

Approved for public release; distribution is unlimited.

See additional restrictions described on inside pages

STINFO COPY

**AIR FORCE RESEARCH LABORATORY
SENSORS DIRECTORATE
WRIGHT-PATTERSON AIR FORCE BASE, OH 45433-7320
AIR FORCE MATERIEL COMMAND
UNITED STATES AIR FORCE**

NOTICE AND SIGNATURE PAGE

Using Government drawings, specifications, or other data included in this document for any purpose other than Government procurement does not in any way obligate the U.S. Government. The fact that the Government formulated or supplied the drawings, specifications, or other data does not license the holder or any other person or corporation; or convey any rights or permission to manufacture, use, or sell any patented invention that may relate to them.

This report is the result of contracted fundamental research deemed exempt from public affairs security and policy review in accordance with SAF/AQR memorandum dated 10 Dec 08 and AFRL/CA policy clarification memorandum dated 16 Jan 09. This report is available to the general public, including foreign nationals.

Copies may be obtained from the Defense Technical Information Center (DTIC) (<http://www.dtic.mil>).

AFRL-RY-WP-TR-2017-0199 HAS BEEN REVIEWED AND IS APPROVED FOR PUBLICATION IN ACCORDANCE WITH ASSIGNED DISTRIBUTION STATEMENT.

// Signature//

JOUNG C. HA, Program Manager
Navigation and Communication Branch
Spectrum Warfare Division
Sensors Directorate

// Signature//

JEFFREY M. HERBERT, DR-4
Chief, Navigation and Communication Branch
Spectrum Warfare Division
Sensors Directorate

// Signature//

JOHN F. CARR, DR-4
Chief, Spectrum Warfare Division
Sensors Directorate

This report is published in the interest of scientific and technical information exchange, and its publication does not constitute the Government's approval or disapproval of its ideas or findings.

*Disseminated copies will show “//Signature//” stamped or typed above the signature blocks.

REPORT DOCUMENTATION PAGE

*Form Approved
OMB No. 0704-0188*

The public reporting burden for this collection of information is estimated to average 1 hour per response, including the time for reviewing instructions, searching existing data sources, gathering and maintaining the data needed, and completing and reviewing the collection of information. Send comments regarding this burden estimate or any other aspect of this collection of information, including suggestions for reducing this burden, to Department of Defense, Washington Headquarters Services, Directorate for Information Operations and Reports (0704-0188), 1215 Jefferson Davis Highway, Suite 1204, Arlington, VA 22202-4302. Respondents should be aware that notwithstanding any other provision of law, no person shall be subject to any penalty for failing to comply with a collection of information if it does not display a currently valid OMB control number. **PLEASE DO NOT RETURN YOUR FORM TO THE ABOVE ADDRESS.**

1. REPORT DATE (DD-MM-YY) January 2018			2. REPORT TYPE Final		3. DATES COVERED (From - To) 3 May 2013 – 31 July 2017	
4. TITLE AND SUBTITLE CHIP-SCALE COMBINATORIAL ATOMIC NAVIGATOR (C-SCAN) Low Drift Nuclear Spin Gyroscope			5a. CONTRACT NUMBER FA8650-13-1-7326			
			5b. GRANT NUMBER			
			5c. PROGRAM ELEMENT NUMBER 62716E			
6. AUTHOR(S) Michael Romalis ()Princeton University Thomas Kornack ()Twinleaf, LLC			5d. PROJECT NUMBER N/A			
			5e. TASK NUMBER N/A			
			5f. WORK UNIT NUMBER Y0VL			
7. PERFORMING ORGANIZATION NAME(S) AND ADDRESS(ES) Princeton University Physics Department Princeton, NJ 08544			8. PERFORMING ORGANIZATION REPORT NUMBER			
9. SPONSORING/MONITORING AGENCY NAME(S) AND ADDRESS(ES) Air Force Research Laboratory,Sensors Directorate Wright-Patterson Air Force Base, OH 45433-7320 Air Force Materiel Command United States Air Force			10. SPONSORING/MONITORING AGENCY ACRONYM(S) AFRL/RYWN		11. SPONSORING/MONITORING AGENCY REPORT NUMBER(S) AFRL-RY-WP-TR-2017-0199	
12. DISTRIBUTION/AVAILABILITY STATEMENT Approved for public release; distribution is unlimited.						
13. SUPPLEMENTARY NOTES This report is the result of contracted fundamental research deemed exempt from public affairs security and policy review in accordance with SAF/AQR memorandum dated 10 Dec 08 and AFRL/CA policy clarification memorandum dated 16 Jan 09. This material is based on research sponsored by Air Force Research laboratory (AFRL) and the Defense Advanced Research Agency (DARPA) under agreement number FA8650-13-1-7326. The U.S. Government is authorized to reproduce and distribute reprints for Governmental purposes notwithstanding any copyright notation herein. The views and conclusions contained herein are those of the authors and should not be interpreted as necessarily representing the official policies of endorsements, either expressed or implied, of Air Force Research Laboratory (AFRL) and the Defense Advanced Research Agency (DARPA) or the U.S. Government. Report contains color.						
14. ABSTRACT We developed a ^3He - ^{129}Xe nuclear spin gyroscope probed by ^{87}Rb atoms. We batch fabricated gyroscope cells with a yield exceeding 85% and achieved ^{129}Xe T ₂ time of 300 sec and ^3He T ₂ time of 3.9 hours in a 2 mm cell. We developed techniques to suppress ^{87}Rb spin-exchange relaxation, ^{129}Xe back-polarization, and ^3He dipolar magnetic field. In a 10 mm cell we achieved Angle Random Walk (AFR) of 0.025 deg/hour $^{1/2}$, bias drift of less than 0.01 deg/hour, and absolute bias of less than 2.5 deg/hour without calibration. In a 2mm diameter anodically bonded cell we achieved ARW of 0.4 deg/hour $^{1/2}$. In a 1.6 cm ³ physics package with the cell, heaters, and VCSEL lasers we demonstrated operation with an ARW of 8 deg/hour $^{1/2}$.						
15. SUBJECT TERMS Gyroscope, nuclear spin, magnetometer, anodically bonded cells						
16. SECURITY CLASSIFICATION OF:		17. LIMITATION OF ABSTRACT: SAR		18. NUMBER OF PAGES 39	19a. NAME OF RESPONSIBLE PERSON (Monitor) Joung Ha	
a. REPORT Unclassified	b. ABSTRACT Unclassified	c. THIS PAGE Unclassified	19b. TELEPHONE NUMBER (Include Area Code) N/A			

Table of Contents

Section	Page
LIST OF FIGURES.....	ii
1.0 SUMMARY.....	1
2.0 FUNDAMENTAL LIMITS ON PRECISION OF NUCLEAR SPIN GYROSCOPES.....	2
2.1 Thermal Diffusion.....	2
2.2 Effects Of Higher Order Magnetic Field Gradients.....	3
3.0 FAST CONTROL OF RB DENSITY.....	5
4.0 TRANSPARENT HIGH THERMAL CONDUCTIVITY MATERIAL FOR CELLS.....	7
5.0 CONSTRUCTION OF ^3He-^{129}Xe-^{87}RB ANODICALLY-BONDED CELLS.....	9
6.0 ACTIVE DEPOLARIZATION OF RB ATOMS.....	13
7.0 ROTATING DEPOLARIZING RF FIELDS TO ELIMINATE BIAS OFFSETS.....	16
8.0 REDUCTION OF DIPOLEAR FIELDS FROM POLARIZED NUCLEAR SPINS.....	18
9.0 OPERATION OF RB MAGNETOMETER.....	19
10.0 PERFORMANCE OF THE GYROSCOPE WITH SPHERICAL CELLS.....	23
11.0 PERFORMANCE OF THE GYROSCOPE WITH ANODIC CELLS.....	26
12.0 PERFORMANCE OF THE GYROSCOPE IN THE PHYSICS PACKAGE.....	27
13.0 ESTIMATES OF FUNDAMENTAL GYROSCOPE SENSITIVITY.....	30
14.0 DEVELOPMENT OF COMPACT FERRITE COIL-SHIELD SYSTEM.....	31
15.0 DISCUSSION AND CONCLUSIONS.....	32
16.0 REFERENCES.....	33
LIST OF SYMBOLS, ABBREVIATIONS, AND ACRONYMS.....	34

List of Figures

Figure	Page
1. Shift in the ratio of ^3He to ^{129}Xe NMR frequency in the presence of linear field gradient.....	3
2. Transverse relaxation for ^3He and ^{129}Xe as a function of second-order magnetic field gradient..	4
3. Shift in the ratio of ^3He and ^{129}Xe frequencies for second-order magnetic field gradient	4
4. Anodically bonded Si glass cell with internal dimensions of 7x7x7mm	5
5. Changes in the Rb density in response to fast changes in the silicon wall temperature	6
6. Illustrations of new anodically bonded geometries enabled by transparency of GaP at 795 nm..	7
7. Picture of a Rb cell with two GaP windows and absorption spectrum of Rb vapor in the cell ...	8
8. Schematic and a picture of the gas handling system for recycling of enriched noble gases	9
9. Wafer of completed gyroscope cells after dicing and one of the separated cells	10
10. Measured Rb magnetic resonance linewidth and prediction for the linewidth	10
11. Spin precession signals in the first generation and second generation cells	11
12. Free spin precession signals for ^3He and ^{129}Xe in anodically bonded cells	12
13. Comparison of three methods for RF depolarization of Rb atoms.....	14
14. Current pulses applied to Helmholtz coils to generate π pulses for Rb depolarization	15
15. ^3He frequency shift due to rotating Rb depolarizing field	16
16. Changes in the frequency ratio as a function of the depolarizing RF amplitude and frequency.	17
17. Changes in the frequency ratio in the presence of nearby copper strip.....	17
18. Changes in the frequency ratio as a function of ^3He projection along bias field	18
19. Rb magnetometer with π pulses and orthogonal pump and probe lasers	19
20. Rb spin signal in response to transverse field and the noise spectrum of Rb magnetometer.....	20
21. Operation of Rb magnetometer in anodically bonded cells and the magnetic noise spectrum... <td>20</td>	20
22. Schematic and photo of the absorption mode magnetometer	21
23. Schematic of the pulse sequence and the noise spectrum of the magnetometer with VCSEL ..	22
24. Timing sequence of the gyroscope measurements and the Allan deviation for Phase I and II...	23
25. Systematic shift in the frequency ratio due to Rb back-polarization and ^3He dipolar fields ..	24
26. Measurements of the absolute Earth rotation for fixed gyroscope orientation	25
27. Allan deviation for 2-mm anodically-bonded cells with in the dark and continuous data.....	26
28. Spectrum of typical gyroscope signal showing Xe and He peaks in the physics package	27
29. Integrated control electronics for the gyroscope operation powered by the USB port	28
30. Gyroscope performance of the physics package	29
31. Time domain and frequency spectrum of the gyroscope signal	30
32. Cylindrical kapton coil and ferrite shield with penetrating wires coil	31

1.0 SUMMARY

In this program we developed a ${}^3\text{He}-{}^{129}\text{Xe}$ nuclear spin gyroscope probed by Rb atoms in a small, anodically bonded, batch fabricated cell.

An important feature of our approach is an absence of unknown bias offsets. We investigated bias offsets due to a number of effects, such as temperature gradients, second-order magnetic field gradients, Rb back-polarization by Xe atoms, frequency shifts due to applied RF fields and due to dipolar magnetic fields from ${}^3\text{He}$. We developed techniques to eliminate each of these bias offsets.

We developed techniques for batch fabrication of gyroscope cells containing enriched isotopes of ${}^3\text{He}$, ${}^{129}\text{Xe}$ and ${}^{87}\text{Rb}$ with a yield exceeding 85%. We constructed a gas recycling system for ${}^3\text{He}$ to avoid wasting this valuable gas during cell filling. We developed reliable cell fabrication procedures and achieved ${}^{129}\text{Xe}$ wall relaxation time of 300 sec and ${}^3\text{He}$ T_2 time of 3.9 hours in a 2 mm diameter, 2 mm height cell, exceeding previous state-of-the-art by a factor of 10-100.

We developed a new technique for operation of the Rb magnetometer that allows suppression of spin-exchange relaxation in a finite magnetic field. We operated the gyroscope using a Ramsey-type interrogation sequence with nuclear spin precession in the dark. We developed techniques for active depolarization of Rb atoms to suppress Xe back-polarization and demonstrated cylindrical cells with a certain aspect ratio that eliminate the dipolar magnetic fields from nuclear spins.

We demonstrated operation of the gyroscope using a 10 mm diameter cell with an Angle Random Walk (ARW) of $0.025 \text{ deg/hour}^{1/2}$ and bias drift of less than 0.01 deg/hour . In 2 mm diameter anodically bonded cells we achieved ARW of $0.4 \text{ deg/hour}^{1/2}$. We demonstrated bias-free operation with absolute bias less than 2.5 deg/hour without calibration.

We developed a compact physics package with a volume of 1.6 cm^3 containing the cell, heaters, VCSEL lasers and photodiodes. In this package we demonstrated operation of the gyroscope with ARW of $8 \text{ deg/hour}^{1/2}$.

2.0 FUNDAMENTAL LIMITS OF A TWO-SPECIES NUCLEAR SPIN GYRO

A nuclear spin gyro operates by measuring the frequencies of precession of two nuclear spin species. By calculating an appropriate combination of their frequencies one can find the inertial rotation rate while eliminating the effects of spin precession due to the magnetic field. In this project we use ^3He and ^{129}Xe atoms because they have spin $I=1/2$ nuclei. Using a 2-level spin system eliminates frequency uncertainties due to the quadrupolar energy shifts and allows one to operate the gyroscope as a clock. From measurements of the frequencies of free spin precession for the two species one can calculate the rotation rate using the known gyromagnetic ratios for ^3He and ^{129}Xe :

$$\omega_{rot} = \frac{\omega_{Xe} - \omega_{He} \gamma_{Xe} / \gamma_{He}}{1 - \gamma_{Xe} / \gamma_{He}} \quad (1)$$

A nuclear spin gyroscope is fundamentally very sensitive to magnetic fields. For example, for ^{129}Xe a rotation bias of 0.01 deg/hour is generated by a magnetic field of 0.65 fT. Two nuclear spin species are always used in nuclear spin gyros to eliminate magnetic field drifts. In principle, if the two spin species occupy exactly the same volume, they will measure exactly the same magnetic field, so it can be perfectly cancelled. However, any non-uniformity in the sampling of the magnetic field by the noble gas coupled to the presence of a magnetic field gradient leads to an imperfect cancellation between the two species. Since magnetic field gradients are usually on the order of 100 pT or more across a cell, one requires gradient cancellation to a part in 10^6 or better.

We have investigated this issue systematically by applying known magnetic field gradients to the cell and measuring the precession frequencies of ^3He and ^{129}Xe . In case of perfect field cancellation, the ratio of their frequencies should remain constant. We have discovered two effects that have not been previously described in the literature.

2.1 Thermal diffusion

Thermal diffusion is an effect which causes the relative density of atoms in a gas mixture to become non-uniform in the presence of a temperature gradient. The effect can be described by a differential equation:

$$\frac{dc_1}{dx} = -k_T \frac{1}{T} \frac{dT}{dx} \quad (2)$$

where c_1 is the relative concentration of one of the gas species and $k_T = D_T/D_{12}$ is the ratio of the thermal diffusion constant D_T to the binary diffusion constant D_{12} . For our conditions with the concentration of ^{129}Xe much smaller than ^3He , the equation can be simplified

$$\frac{\Delta c_1}{c_1} = \alpha_T \frac{\Delta T}{T} \quad (3)$$

where α_T is so-called thermal diffusion factor. For He-Xe the thermal diffusion factor is approximately equal to 1.

To confirm this effect experimentally we have measured the ratio of the ^3He to ^{129}Xe spin precession frequencies while applying a linear magnetic field gradient and a temperature gradient. Non-uniform distribution of ^{129}Xe spins causes the ratio of the spin precession frequencies to become sensitive to the magnetic field gradient. The sign of this dependence changes with the sign of the temperature gradient, a key prediction for the thermal diffusion effect. The results are shown in Fig. 1. Quantitative analysis shows that the size of the gradient frequency shift is consistent with expectations.

The discovery and description of this effect places an important requirement for temperature uniformity across the cell to minimize sensitivity to magnetic field gradients. It can also be responsible for a temperature-dependent bias drift in the presence of a constant magnetic field gradient.

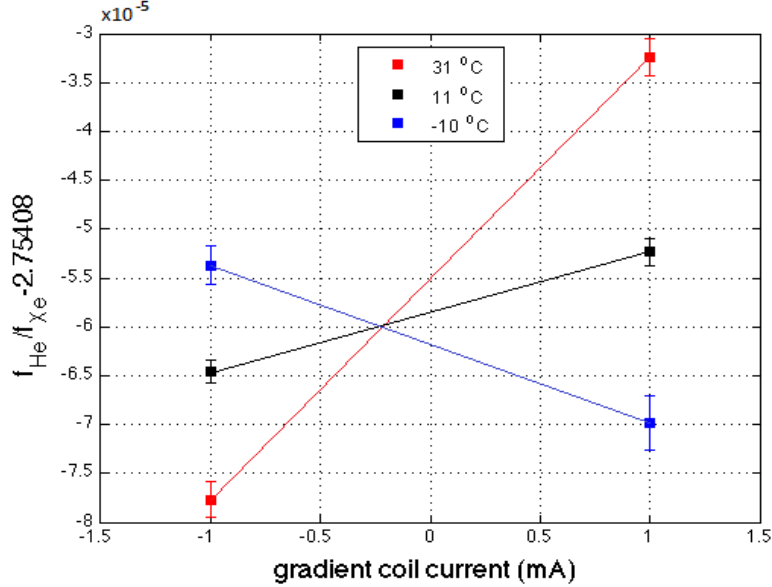


Fig. 1: Shift in the ratio of ${}^3\text{He}$ to ${}^{129}\text{Xe}$ NMR frequency in the presence of a linear magnetic field gradient as a function of the temperature difference across the cell

2.2 Effects of higher order magnetic field gradients

The effects of linear magnetic field gradients on the spin precession frequencies and spin relaxation in a gas cell have been investigated in detail by W. Happer and co-workers [1]. The effects of higher order magnetic field gradients have not been studied systematically despite the fact that in a well-engineered system linear magnetic field gradients should be equal to zero in the vicinity of the cell and only quadratic or quartic gradients are present.

To systematically analyze these effects we have developed a new theoretical model for treatment of spin precession in the presence of diffusion. It allows one to extend the calculations to all orders in magnetic field gradients. Briefly, our approach is based on expanding the Bloch-diffusion equation

$$\frac{\partial \vec{P}}{\partial t} = D \nabla^2 \vec{P} + \gamma \vec{P} \times \vec{B} \quad (4)$$

into normal diffusion modes. The magnetic field inside the cell is derived from a gradient of a scalar magnetic potential $\vec{B} = \nabla \Phi$, which is expanded in spherical harmonics

$$\Phi = \sum_{l=1}^L \sum_{m=-l}^l A_{lm} r^l Y_{lm}(\theta, \phi) \quad (5)$$

In this approach $l=1$ terms correspond to the three uniform magnetic fields, $l=2$ terms to five independent linear magnetic field gradients, $l=3$ terms to seven independent quadratic magnetic field gradients and so on. Magnetic field gradients of arbitrary order can be included while preserving the source-free nature of magnetic fields inside the cell.

We have investigated several new effects using our theoretical approach, which also reproduces all results derived in [1]. Fig. 2 shows the transverse relaxation rate due to the second-order magnetic field gradient. The model reproduces the data without any adjustable parameters.

We also discovered that second-order magnetic field gradients can lead to shifts in the ratio of ^3He to ^{129}Xe precession frequencies. This is due to the fact that they induce non-uniform spin relaxation in the cell, creating a polarization gradient. The results of our measurements of this effect are shown in Fig. 3. Interestingly, the frequency shift is proportional to the third power of the magnetic field gradient.

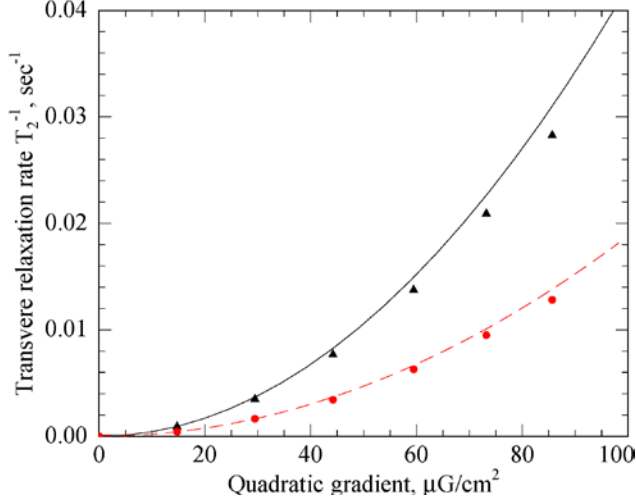


Fig. 2: Transverse relaxation rate for ^3He (black) and ^{129}Xe (red) as a function of second-order magnetic field gradient d^2B_z/dz^2 , lines are theoretical predictions without free parameters

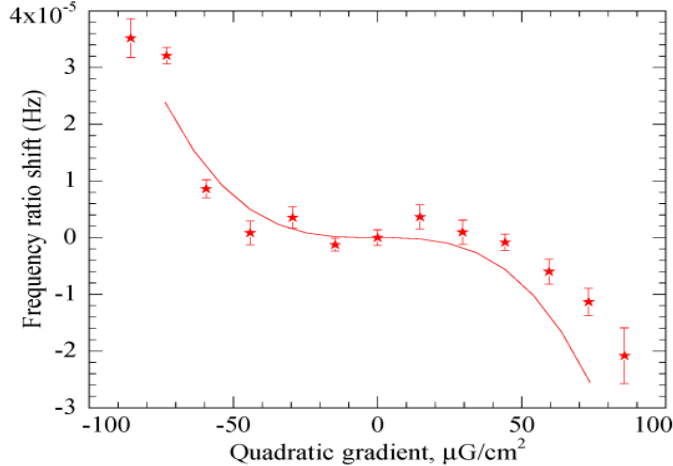


Fig. 3: Shift in the ratio of He and Xe precession frequencies as a function of the second order magnetic field gradient, the solid curve shows theoretical prediction without any free parameters

We find that the frequency shift due to second-order magnetic field gradients is significantly suppressed for $^3\text{He}-^{129}\text{Xe}$ mixture because the ratio of their diffusion constants is approximately equal to the ratio of their gyromagnetic ratios, $D_{\text{He}}/D_{\text{Xe}} \approx \gamma_{\text{He}}/\gamma_{\text{Xe}}$. The effect would vanish if that equality were exact.

This effect points to a significant sensitivity of nuclear spin gyroscopes to second order magnetic field gradients. Also other local gradients, such as due to magnetic impurities in the cell walls, can contribute to the bias drift of the gyroscope. The results of our studies are published in [2]. They provide tools for quantitative engineering modelling of nuclear spin gyroscopes.

3.0 FAST CONTROL OF ALKALI-METAL DENSITY

We investigated the fundamental limitations for a fast control of Rb density in the vapor cells. It can be used for fast initial start-up of the gyroscope or to remove Rb vapor from the cell during free nuclear spin precession interval. For this purpose we made anodically-bonded cells with glass and silicon walls, so we can control their temperature separately. Fig. 4 shows a picture of such cell. Silicon has a much higher thermal conductivity than glass, allowing faster changes in the cell wall temperature.



Fig. 4: Anodically bonded Si-glass cell, the internal dimensions of the cell are 7x7x7 mm and the glass walls are 2 mm thick

The data for the density as a function of time are shown in Fig. 5. We used TECs to quickly change the temperature of the silicon walls and measured transmission of a laser passing through the cell. A number of interesting features are observed in this data.

When the glass walls of the cell are not specifically heated (see Fig. 5a) the density of Rb follows the glass temperature while the cell is heated, but follows the silicon temperature when it is cooled. This can be understood by assuming that during heating most Rb atoms evaporating from the silicon walls are absorbed by the glass until the Rb density is in equilibrium with the glass temperature. In contrast, during cooling, Rb atoms evaporating from the glass surface are condensed on the silicon surface. In other words, the Rb density follows the temperature of the coldest surface.

In Fig. 5b) we show the case when the glass walls of the cell are held at an elevated temperature compared to silicon by additional heating. In this case, Rb density follows the silicon surface temperature for both heating and cooling. As long as silicon is the coldest surface, it can be used to quickly control the Rb density. Note that even small fast features of the temperature, such as PID oscillations, are reproduced in the Rb density, so there is no significant low-pass filtering.

This study points to two possible directions to achieve fast control of Rb density. It is sufficient to use a relatively small fraction of the cell surface that is quickly cooled and heated to control the Rb density. But the rest of the cell walls have to be maintained at a higher temperature, for example by laser heating. This has potential negative implications for the power consumption of the device.

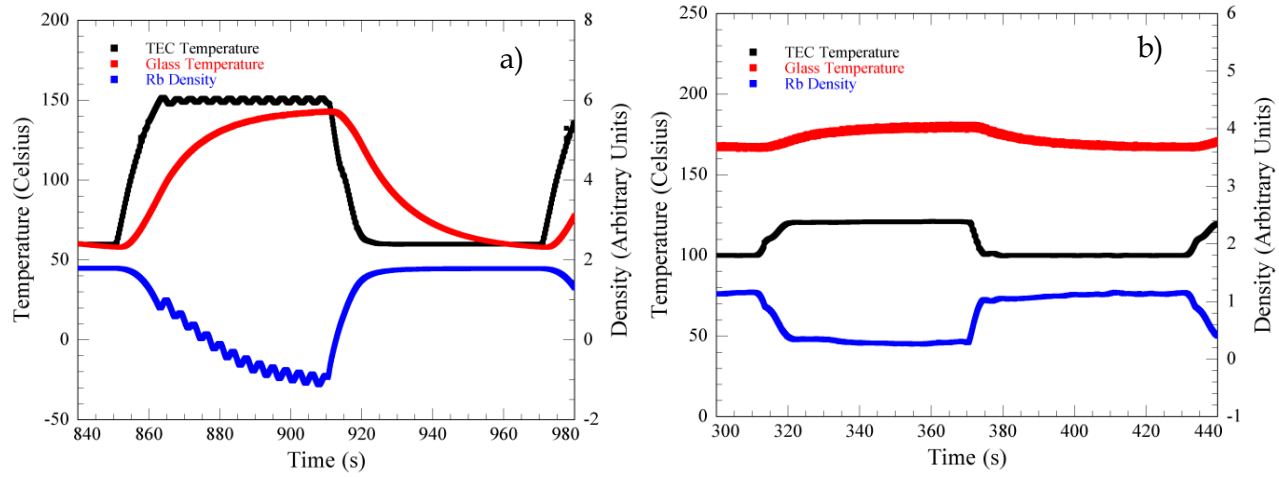


Fig. 5: Changes in the Rb density in response to fast changes of the silicon wall temperature:
a) the glass walls of the cell are not heated and b) the glass walls of the cell are always kept
at a higher temperature than silicon walls

4.0 GAP AS A NEW TRANSPARENT HIGH THERMAL CONDUCTIVITY MATERIAL FOR CELL CONSTRUCTION

The second approach for fast control of Rb density is to use materials with high thermal conductivity for all sides of the cell. To this end we have looked for high thermal conductivity transparent materials that can be used for cell construction. High thermal conductivity is also important for maintaining a uniform temperature across the cell during spin precession measurements, since temperature gradients lead to systematic effects due to the thermal diffusion effect. The material has to be non-birefringent, stable against alkali-metal and amenable to common bonding techniques. Among possible choices we focused on GaP, which is a semiconductor with a band gap of 2.2 eV, so it is transparent to near-infrared radiation. GaP has thermal conductivity similar to silicon and nearly 70 times larger than glass. It also has a thermal expansion coefficient not that different from silicon and Pyrex, so it can be used for anodic bonding. Furthermore, GaP is not permeable to He gas because it is a single crystal.

Because GaP is transparent in the near infrared, it allows fundamentally different geometries for anodically bonded cells, as illustrated in Figure 6. One can construct cells using only high thermal conductivity materials and potentially arrange for optical access from all six sides.

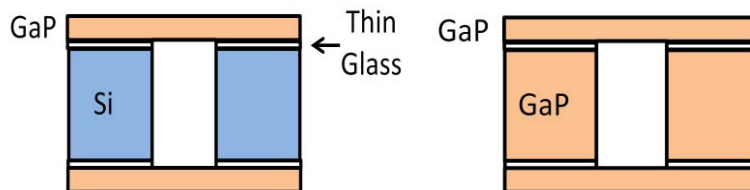


Figure. 6: Illustrations of new anodically bonded geometries enabled by transparency of GaP at 795 nm.

We have performed a number of tests to determine the properties of GaP relevant for alkali-metal cell fabrication. We found that anodic bonding between Pyrex and GaP can be completed at temperatures as low as 150°C, significantly lower than between Silicon and Pyrex. This is important because the thermal expansion coefficient for GaP is $4.8 \times 10^{-6}/\text{K}$, higher than for Silicon and Pyrex. We developed a single-layer Al₂O₃ anti-reflection coating for GaP, so that transmission of the laser at 795 nm is greater than 95%. We also find that Al₂O₃ coating improves the chemical resistance of GaP to the Rb vapor. We found that anodic bonding can be performed through the anti-reflection coating, simplifying fabrication of the cells. Fig. 7 shows a picture of one of the cells and the spectrum of absolute transmission through the cell, including losses on windows. We also verified that permeability of He gas through GaP is at least 100 times lower than through Pyrex. This also makes GaP a good candidate for vacuum windows where permeation of atmospheric helium into the system through glass windows is a problem. The results of our studies of GaP are published in [3].

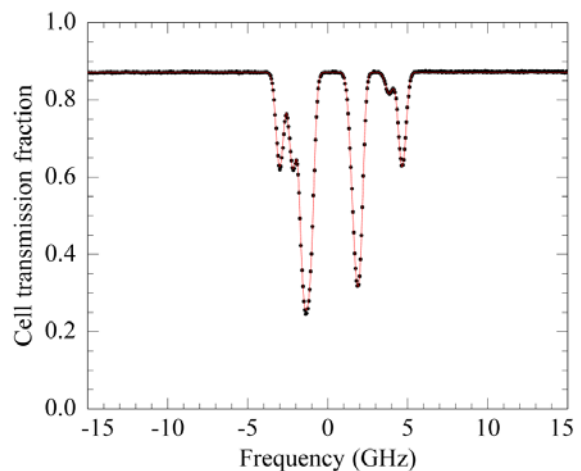
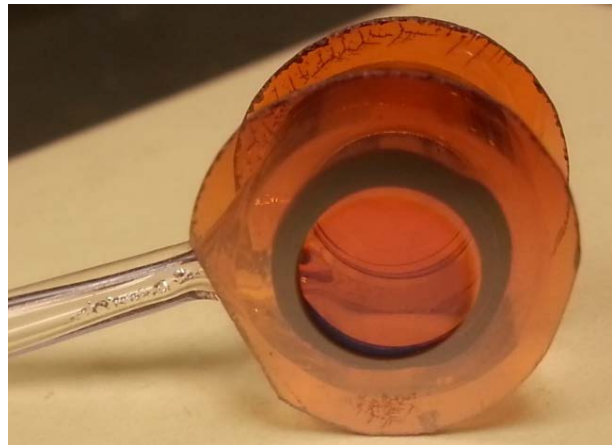


Fig. 7 Picture of a Rb cell with two GaP windows anodically bonded to Pyrex cell body and the absorption spectrum of Rb measured through two GaP windows with Al_2O_3 coating on all surfaces, the red line is a fit to a Doppler profile

5.0 CONSTRUCTION OF ${}^3\text{He}$ - ${}^{129}\text{Xe}$ - ${}^{87}\text{RB}$ ANODICALLY-BONDED CELLS

A significant effort was devoted to fabrication of gyroscope cells. Two main challenges have been solved for the first time. The first is fabrication of anodically bonded cells containing enriched nuclear spin isotopes, particularly ${}^3\text{He}$. The second is production of small anodically bonded cells with very long nuclear spin relaxation times.

In a typical system for making anodically-bonded cells the whole bonding system volume is filled with gases prior to bonding. This results in a very inefficient use of enriched gas isotopes, since the volume of the cells is a tiny fraction of the system volume. Therefore, we constructed an anodic bonding system that enables recycling of the gas, so the same enriched noble gas can be reused many times. Furthermore, several redundancy features are included to avoid the possibility of venting scarce ${}^3\text{He}$ to the atmosphere in case of a system malfunction.

The gas handling manifold uses a simple cryogenic system to purify and store the gasses used for cell fabrication. A transfer and storage line is placed into a liquid helium dewar to cryopump the gasses. At the end of the dipper is a copper section of tube filled with charcoal to efficiently cryopump ${}^3\text{He}$ at 4 K. After all the gasses have been cryopumped into this small volume, the transfer line may be valved off and allowed to warm up to room temperature. The volume is designed to withstand a pressure of 1500 psi that is reached when all gases are condensed inside. It may be necessary to purify the ${}^3\text{He}$ on occasion so we have added a liquid nitrogen cold trap. In case liquid helium is lost and the cryopumping is ineffective, the entire volume of gas may be pumped out and stored in a temporary 30L storage tank using a sealed scroll pump. The system diagram and photo are shown in Fig. 8.

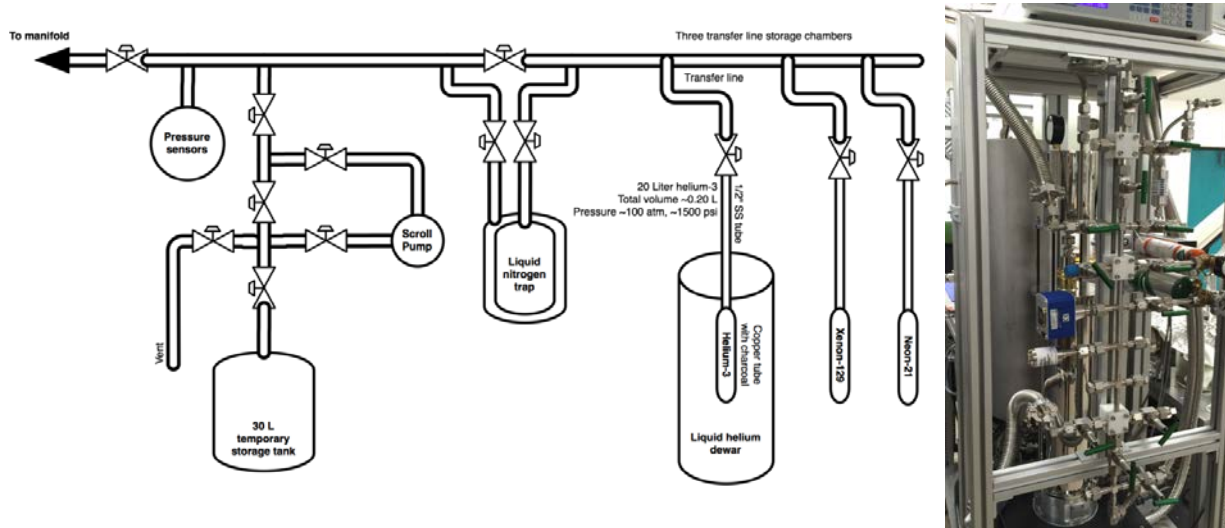


Figure 8. Schematic and a picture of the gas handling system for recycling of enriched noble gases.

The cells are fabricated using a 2 mm thick silicon wafer drilled with 2 mm diameter cylindrical holes and sealed using an anodically-bonded cover glass. The wafer size was 32 mm square with a

7×7 array of holes. Fig. 9 shows the wafer after dicing of the finished cells and one of the separated cells.

Several successful wafers were fabricated throughout the research program. The cell yield for a typical wafer is 85% or more. To reduce ^3He diffusion through the cell walls, we used an aluminosilicate cover glass. An accelerated aging test at 210°C demonstrated that the aluminosilicate glass cells did not lose a significant quantity of helium. The viewports of the anodic bonding system are made to withstand about 2 atm pressure, which determines the maximum ^3He pressure that can be put into the system before anodically sealing the cells. The cells typically contain enriched ^{87}Rb , about 1400 Torr of ^3He , 6.5 Torr ^{129}Xe and 75 Torr of N_2 . After sealing and dicing the cells, heat is applied to glass windows to drive Rb metal condensation to the side walls.



Fig. 9: Wafer of completed gyroscope cells after dicing and one of the separated cells.

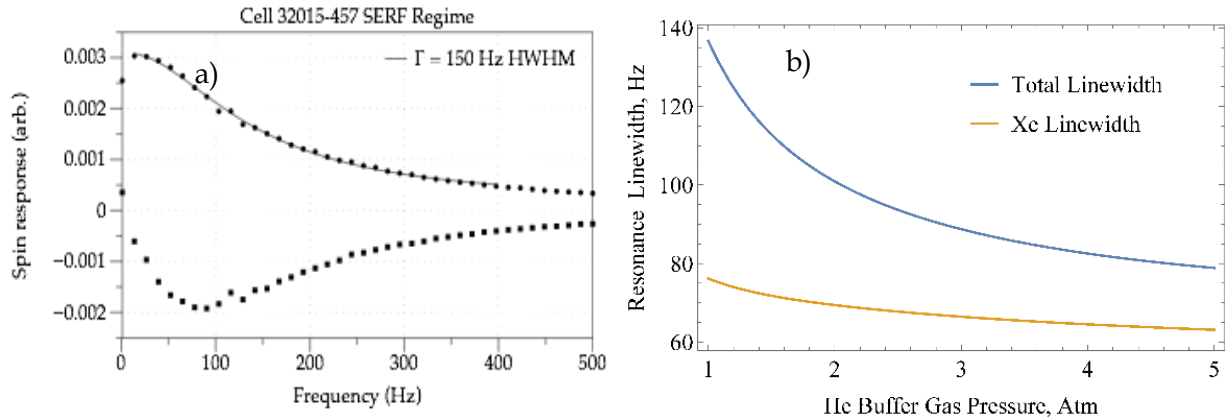


Figure 10. a) Measured Rb magnetic resonance linewidth at low pump power. b) Prediction for the resonance linewidth as a function of He buffer gas pressure for 6.5 torr of ^{129}Xe .

In Fig. 10 we show the measured magnetic resonance lineshape of Rb atoms in an anodically-bonded cell, which provides a measure of the ^{87}Rb transverse relaxation time. The resonance linewidth of about 100 Hz, which is in good agreement with predictions based on the relaxation cross-sections and diffusion of Rb atoms. In a 2 mm cylindrical cell, the power required to pump the Rb atoms to 50% spin polarization is approximately 150 μW . The transverse relaxation time of Rb can be improved by about a factor of two by increasing the pressure of He in the cell to about 5 atm. to reduce the rate of diffusion of Rb atoms to the cell walls and simultaneously reducing the

pressure of Xe to about 3 torr. This would reduce the required laser power by a factor of two and bring the ratio of He to Xe signal amplitudes closer to the optimum.

Another major challenge in the fabrication of the cells was in achieving long spin relaxation times. In the first generation of cells we obtained a spin relaxation time for ^{129}Xe of only a few seconds, as shown in Fig. 11a). The time-zoomed insets above the plot show the presence of two frequencies (^3He and ^{129}Xe) at early times and only ^3He frequency at later times.

We performed several experiments to study the dependence of the ^{129}Xe lifetime on the materials used in cell construction. However, we found that the most important factor in the ^{129}Xe spin lifetime was related to the temperature of the cell bake-out prior to filling. Using spherical aluminosilicate glass blown cells we have achieved a ^{129}Xe T_2 lifetime of 1000 sec by baking the cells for a week at 550°C, as shown in Fig. 11b).

A similar bake out procedure was developed for the anodically bonded cell. This process was continuously improved, so the last batch of anodically bonded cells fabricated at Twinleaf achieved a ^{129}Xe transverse relaxation time of 300 sec and a ^3He transverse relaxation time of 3.9 hours, as illustrated in Fig. 12.

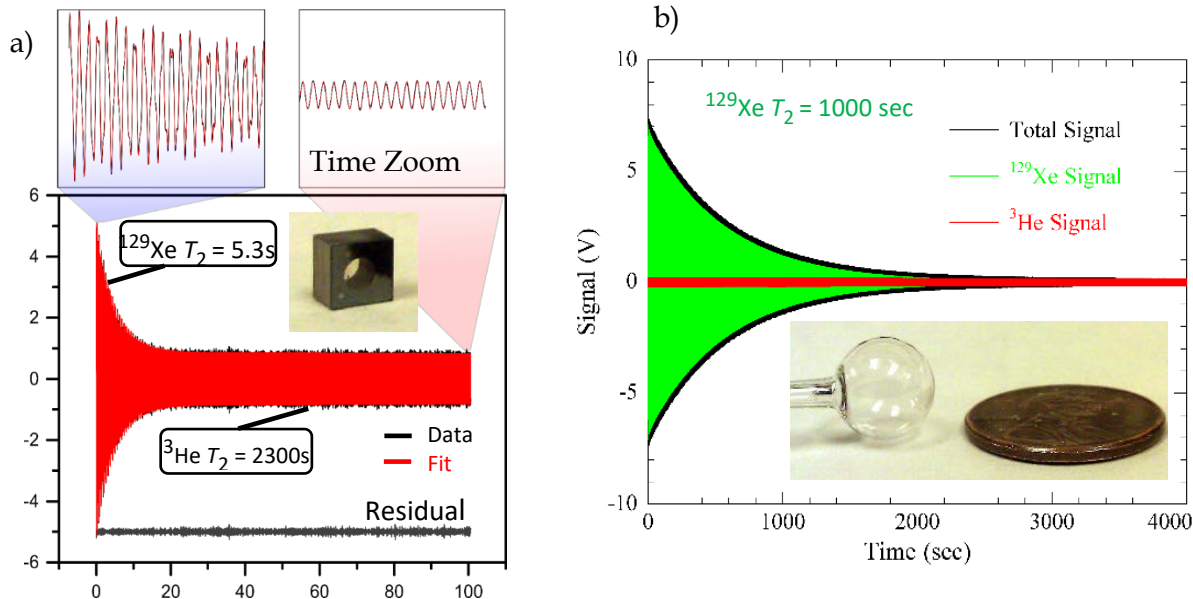


Fig. 11. a) Spin precession signals in the first generation of anodically-bonded cells and b) spin precession signals in spherical glass-blown cells with high temperature baking. Insets above show the time zoom of the signal with ^3He and ^{129}Xe frequencies

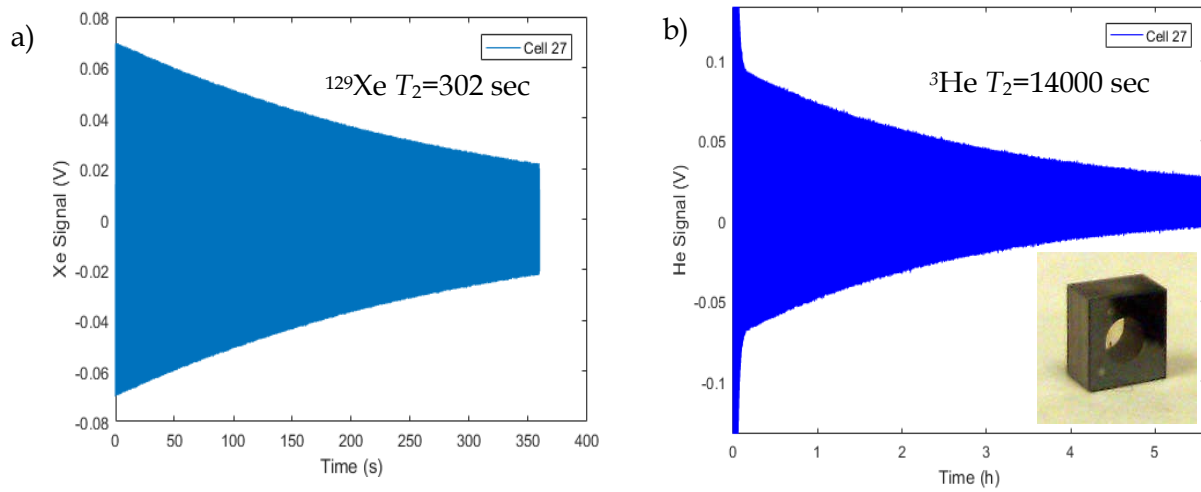


Fig. 12: Free spin precession signals for a) ^{129}Xe and b) ^3He in one of the anodically-bonded cells

6.0 ACTIVE DEPOLARIZATION OF RB ATOMS

Using nuclear spins with $I=1/2$, such as ^3He and ^{129}Xe , we can achieve long spin relaxation times and elimination of quadrupolar energy shifts. However, it also presents challenges in operation of the gyroscope because of magnetic fields created by polarized Rb atoms. The frequency shift experienced by nuclear spins is given by

$$\Delta\omega = \gamma\kappa_0 \frac{8\pi}{3} \mu_e n_{Rb} P_{Rb} \quad (6)$$

where γ is the gyromagnetic ratio and κ_0 is the contact interaction factor for each of the nuclear spins. μ_e is the electron magnetic moment, n_{Rb} and P_{Rb} are the density and polarization of Rb atoms. Since the κ_0 factor is very different for ^3He and ^{129}Xe , 5.6 vs. 490, this frequency shift does not cancel between the two nuclear spin species. Under typical conditions, with 50% Rb polarization, the frequency shift for ^{129}Xe atoms corresponds to about 160 degrees/sec bias offset. Therefore, this frequency shift needs to be suppressed by a factor of more than 10^8 . Even for nuclear spin gyroscopes using the two isotopes of Xe there is a difference in the values of κ_0 of about 0.2% [4]. So one needs a method for reducing the Rb polarization shift by a factor of 10^5 .

Here we use the approach of a Ramsey clock interrogation scheme, where the optical pumping, free evolution, and measurement intervals for nuclear spins are separated in time. During the free evolution period instead of optical pumping we actively depolarize Rb atoms to bring their polarization close to zero. Another way to reduce the Rb frequency shift is to reduce the Rb density during free precession. We have looked at the practical approaches for fast control of the Rb density, but they would generally significantly increase the power consumption needed for heating.

The active depolarization of Rb atoms is necessary because even if the pump lasers are turned off, the Rb atoms become back-polarized by spin-exchange with ^{129}Xe . The degree of back-polarization is given by

$$P_{Rb} = \frac{k_{se} n_{Xe} P_z^{Xe}}{R_{Rb}} \quad (7)$$

where k_{se} is the Rb-Xe spin exchange rate, n_{Xe} is density of Xe, P_z^{Xe} is the Xe polarization along the bias field and R_{Rb} is the Rubidium spin relaxation rate. During the free precession interval the Xe polarization along the z axis is nominally zero, but may be on the order of 1% of the initial Xe polarization if the tipping pulse is not accurate. The initial Xe polarization created during the pumping interval is about 10%. The ratio $k_{se}n_{Xe}/R_{Rb}$ is about 0.02, based on the measured relaxation rates. Thus, the Rb polarization created in the absence of optical pumping is on the order of $P_{Rb}=2\times 10^{-5}$. Therefore, we need to actively suppress the Rb polarization by 4 orders of magnitude to bring this source of bias offset to a level of 0.001 deg/hour.

During the course of this project we investigated three methods for active depolarization. We used a CW RF field tuned to the Rb Zeeman resonance, an RF field tuned to the hyperfine resonance frequency of alkali-metal atoms, and a series of π RF pulses applied to the Rb spins. Fig. 13 shows a comparison of their performance. With CW RF and microwave fields we were able to achieve a

depolarization factor of 100 to 300. Using a series of π pulses for Rb atoms we measured a depolarization factor of 5×10^3 . These results are in agreement with theoretical calculations, and we expect that a factor of 10^4 will be possible using π pulse rate of 2×10^5 Hz and pulse duration of less than 1 μ sec.

To implement the π pulse depolarization scheme we developed a bipolar current driver that is able to generate 1-2 A current pulses with a rise time of less than 1 μ sec and low current noise between the pulses. The current pulses flow through a separate set of Helmholtz coils with a 3 μ H inductance to generate a field of about 1G at the location of the cell.

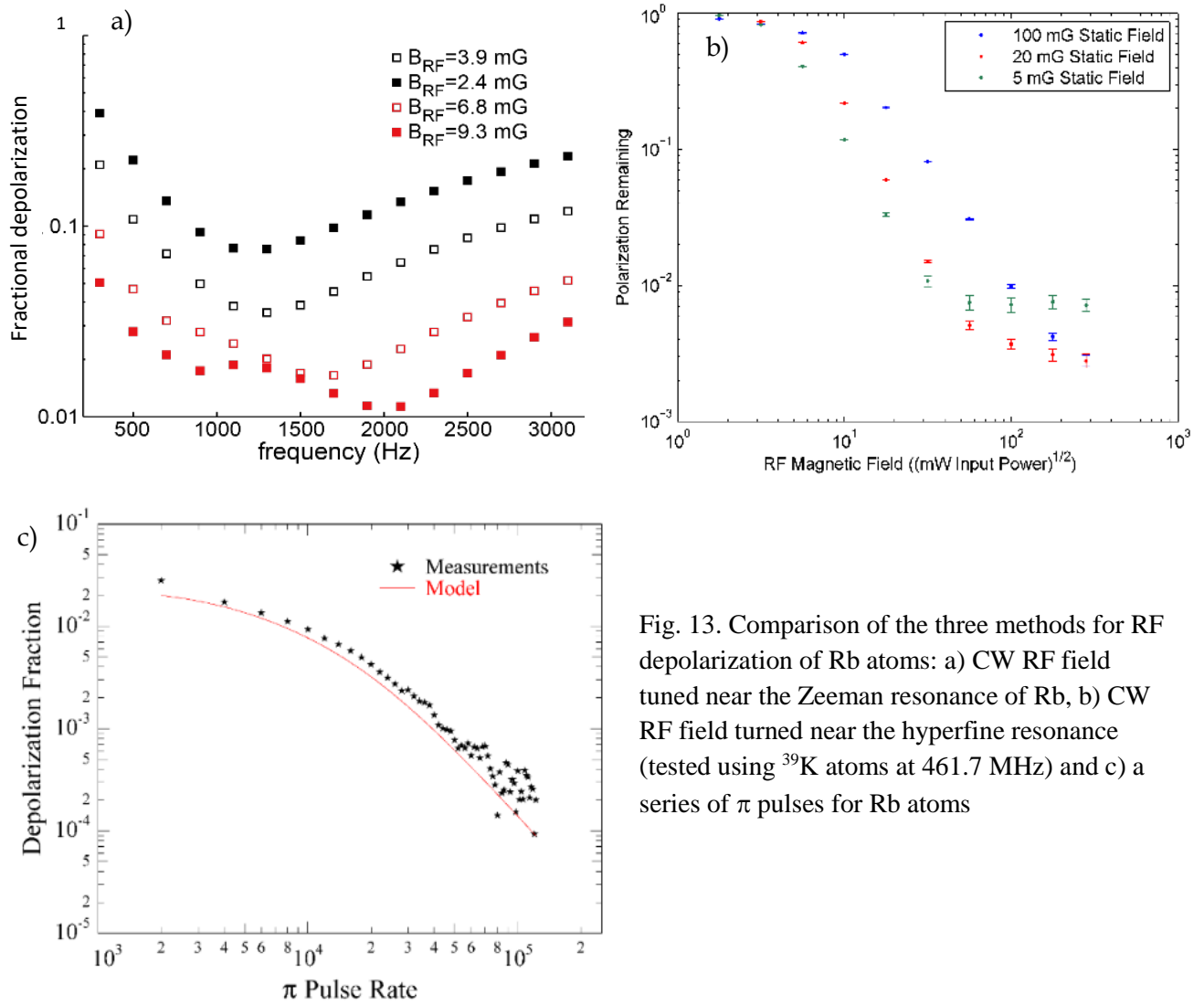


Fig. 13. Comparison of the three methods for RF depolarization of Rb atoms: a) CW RF field tuned near the Zeeman resonance of Rb, b) CW RF field turned near the hyperfine resonance (tested using ^{39}K atoms at 461.7 MHz) and c) a series of π pulses for Rb atoms

To generate the current we used an LT1210 high current op-amp in a current source configuration or an Apex PB63 high voltage power booster as a voltage source to drive the coils through a 50Ω resistor. The pulses themselves are generated using ADG1223 CMOS switches from a stable voltage source. Several iterations of the pulse boards have been fabricated by Twinleaf based on the

initial design developed at Princeton. Fig. 14 shows an example of the current pulses. The pulses follow $\pi, \pi, -\pi, -\pi$ sequence to average the effects of pulse field gradients.

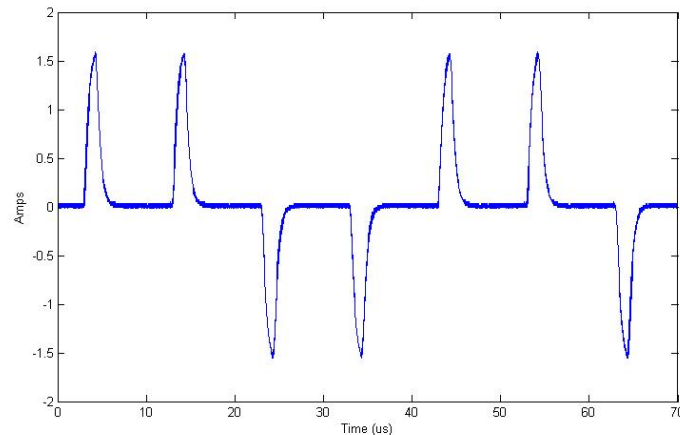


Fig. 14: Current pulses applied to Helmholtz coils to generate a series of π pulses for Rb depolarization

7.0 ROTATING DEPOLARIZING RF FIELDS TO ELIMINATE BIAS OFFSETS.

The RF depolarizing field used to control the polarization of Rb atoms can also introduce frequency shifts for nuclear spins through off-resonant Bloch-Siegert type shifts. If we use a CW depolarizing RF field, the frequency shift is given by

$$\delta\omega = \gamma B_0 \left(\frac{\gamma B_{RF}}{2\omega_{RF}} \right)^2 \quad (8)$$

so for the Zeeman RF depolarization approach the frequency shift is about 0.3 deg/sec. This frequency shift primarily affects ^3He atoms because they have a larger gyromagnetic ratio γ . In the case of depolarization with π pulses, the frequency shift is given by

$$\delta\omega = \gamma B_0 \left(\frac{\gamma\pi}{2\gamma_{Rb}} \right)^2, \quad (9)$$

which gives a similar size effect.

In order to eliminate these effects we developed a general method of using a slowly rotating depolarizing field. If the plane of the depolarizing field (either CW or π pulses) is rotating, the frequency shift for CW field becomes

$$\delta\omega = (\gamma B_0 - \omega_{rot}) \left(\frac{\gamma B_{RF}}{2\gamma\omega_{RF}} \right)^2 \quad (10)$$

and similar for the π pulse field. If the plane of the field rotates at the frequency matching the nuclear spin precession frequency, it does not generate any Bloch-Siegert shift. In our case we care about the ratio of the two nuclear spin precession frequencies. One can generally show that if the depolarizing field is rotating at the sum of their precession frequencies, $\omega_{rot} = (\gamma_{\text{He}} + \gamma_{\text{Xe}})B_0$, it will not generate any effect on the ratio of their frequencies. Fig. 15 shows some of the early data and calculations demonstrating the basic effect. The ^3He precession frequency is shifted approximately as the square of the RF field amplitude. However, the sign of the shift can be reversed by rotating the plane of the π pulses.

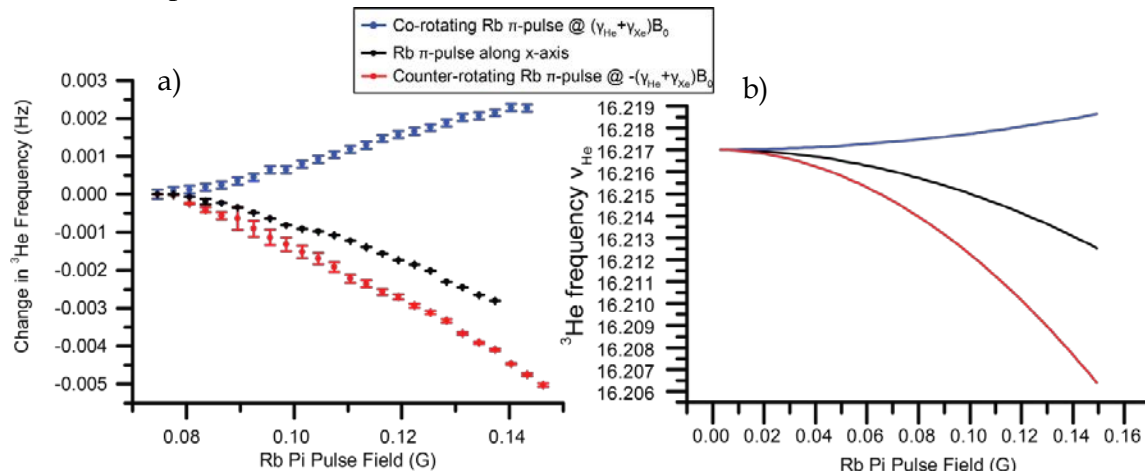


Fig. 15: ^3He frequency shift due to Rb rotating depolarizing field, a) experimental data and b) theoretical simulations

We use this method during the nuclear spin free evolution time interval, the Rb spins are actively depolarized by a rotating field. Fig. 16 shows the efficiency of this technique in eliminating changes in the nuclear spin precession frequency ratio due to the depolarizing field. The frequency ratio does not change with the amplitude of the depolarizing field when the rotation rate matches the sum of the nuclear spin precession frequencies. The sense of rotation should be reversed together with the magnetic field, so that it follows the sense of nuclear spin precession.

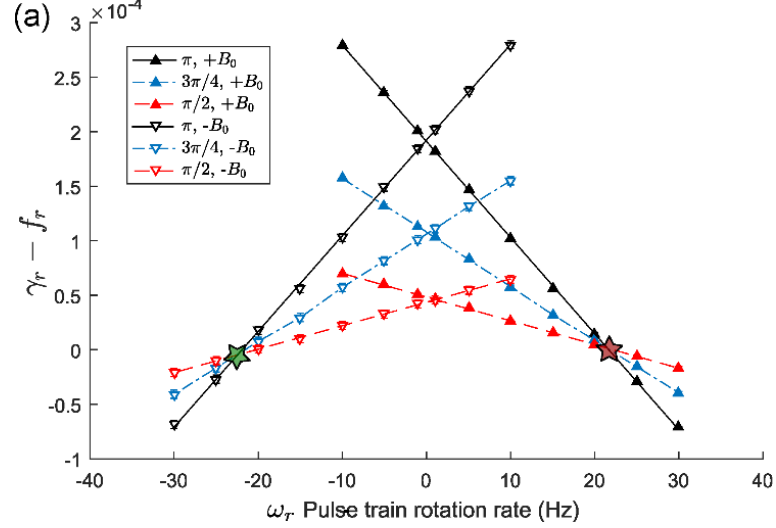


Fig. 16: Changes in the nuclear spin precession ratio $\gamma_{\text{He}}/\gamma_{\text{Xe}} - \omega_{\text{He}}/\omega_{\text{Xe}}$ as a function of the depolarizing pulse amplitude ($\pi/2, 3\pi/4, \pi$) and the frequency of the plane rotation; at the proper rotation frequencies (denoted by stars), there is no shift in the frequency ratio

Experimentally, the plane of the depolarizing field is rotated by utilizing two orthogonal magnetic field coils and driving them with $\cos(\omega_{\text{rot}} t)$ and $\sin(\omega_{\text{rot}} t)$ amplitudes. During investigation of these effects we found that the frequency shift depends sensitively on the fact that the depolarizing field of each pulse is planar. If we introduce large electrical conductors close to the cell, they generate eddy currents which cause the magnetic field of each pulse to develop a certain rotation sense. This can introduce a significant additional frequency shift, as illustrated in Fig. 17.

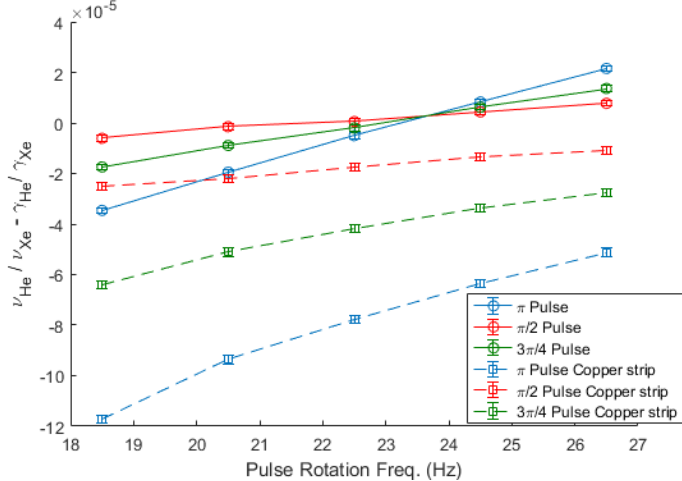


Fig. 17: Change in the frequency ratio as a function of the pulse plane rotation frequency; introduction of a copper strip near the cell causes the frequency ratio to shift significantly

8.0 REDUCTION OF DIPOLEAR FIELDS FROM POLARIZED NUCLEAR SPINS

Another source of bias offset comes from dipolar fields created by nuclear spins. This effect affects all nuclear spin gyroscopes to some extend because polarized nuclear spins create an appreciable magnetization. The polarized nuclear spin magnetic moments inside the cell can be treated as a uniform magnetization. The average magnetic field due to the uniform magnetization depends on the geometrical shape of the cell. In particular, if the cell is perfectly spherical this effect would average to zero. In practice, spherical cells are usually hand-blown and have significant imperfections and a filling stem.

In our approach the dipolar frequency shifts are suppressed by tipping the nuclear spins by exactly 90 degree relative to the bias field prior to free evolution. The shift in the nuclear spin precession frequency ratio as a function of the tipping angle is shown in Fig. 18a). When the ${}^3\text{He}$ polarization is exactly in the transverse plane, the dipolar frequency shift vanishes. One can also see that the slope of the frequency shift vs. angle is similar in a cylindrical anodically-bonded cell and in a nominally spherical glass-blown cell.

The frequency shift can be suppressed even further by changing the aspect ratio of the cylindrical cells. In general, the dipolar field from uniform magnetization has opposite sign in the pancake-shaped and cigar-shaped cells, so there is a particular aspect ratio where the dipolar fields cancel. Fig. 18b) shows the slope of the frequency ratio shift per ${}^3\text{He}$ magnetization as a function of the cylindrical cell height. To make these measurements Twinleaf fabricated a special wafer with a slight wedge, so cells in different rows of the wafer have different heights. Making measurements of the dipolar shift in several cells allows us to find the optimal height of the cylinder, near 1.72 mm, where the dipolar effects are cancelled for cells with a diameter of 2.00 mm. Anodically bonded cells with no stem have a high degree of reproducibility, so the geometrical dipolar effects can be cancelled consistently.

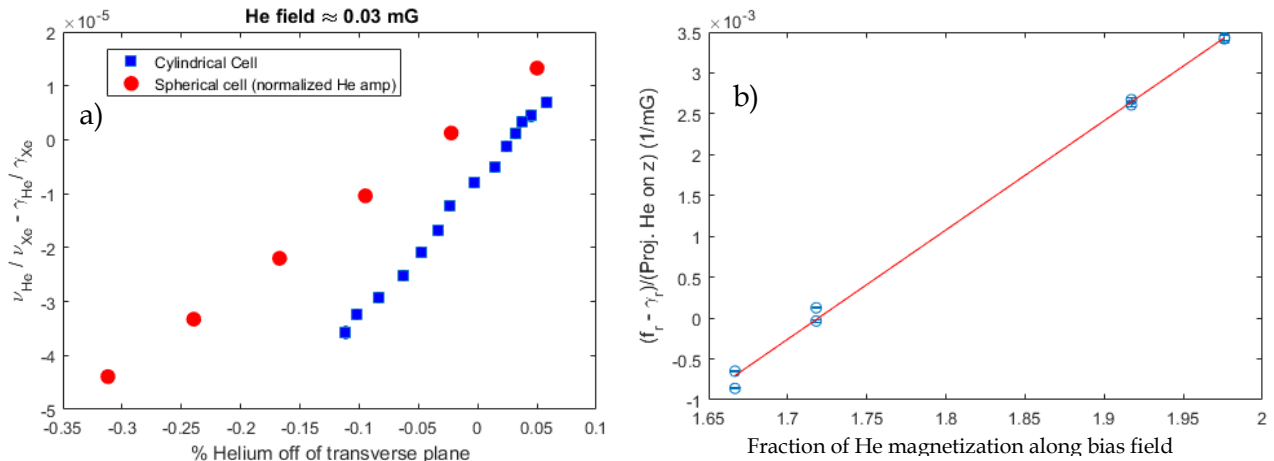


Fig. 18. a) Changes in the nuclear spin frequency ratio as a function of ${}^3\text{He}$ projection along the bias field and b) changes in the frequency ratio as a function of the cylindrical cell height for a cell diameter equal to 2.00 mm.

9.0 OPERATION OF RB MAGNETOMETER

The short term sensitivity of the gyroscope are determined in part by the sensitivity of the Rb magnetometer. The Rb magnetometer sensitivity is determined by the spin relaxation rate as well by the operation mode of the readout process. We have developed three methods for readout of the Rb signals, two relying on the π pulses and one on an alternative field modulation technique.

For measurements in spherical cells we use orthogonal pump and probe lasers, as shown in Fig. 19. We apply the π pulse sequence along the y axis, perpendicular to pump and probe lasers. The role of π pulses is three-fold in this case. They prevent Rb polarization build-up along the bias field, they allow the Rb magnetometer to sense the transverse magnetic field generated by the precessing nuclear spins, and they reduce relaxation due to spin-exchange collisions in Rb vapor.

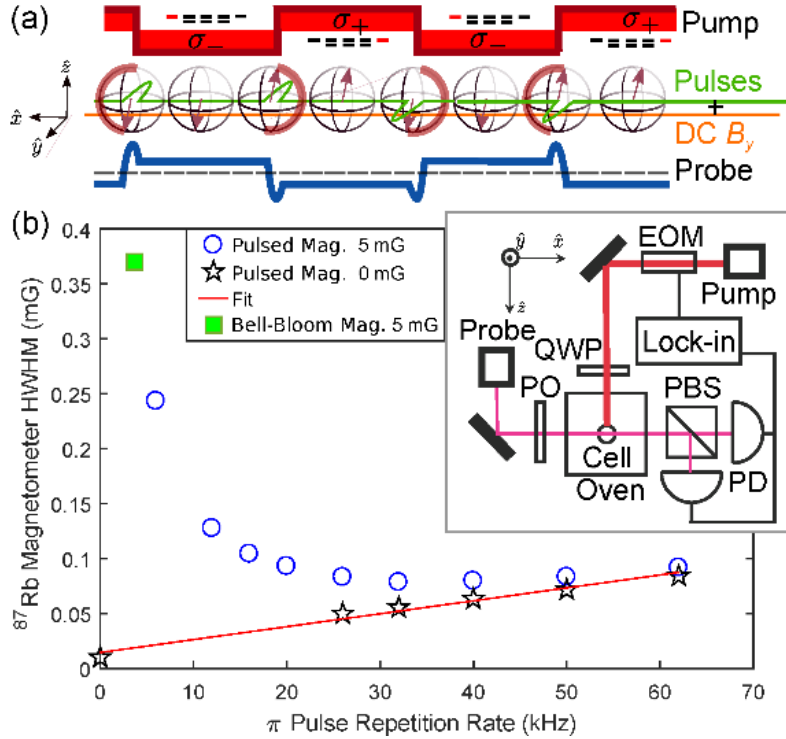


Fig. 19: Rb magnetometer with π pulses and orthogonal pump and probe lasers; panel a) shows the modulation of the pump light polarization synchronous with the π pulses, panel b) shows the suppression of spin-exchange collisions, the inset shows the basic experimental setup

In Fig. 19b) we show the Rb resonance linewidth as a function of the rate of the π pulses. Increasing the rate of the pulses reduces the linewidth by suppressing the relaxation due to the Rb spin-exchange collisions. This effect can be understood by noting that the gyromagnetic ratios have opposite signs in the two hyperfine states of Rb atoms. The spins precess in opposite directions in the bias magnetic field B_0 . The π pulses prevent the precession in B_0 field by refocusing the spins, so the expectation value of the polarization remains the same in both hyperfine states. This allows the magnetometer to operate as if it were in a zero-field spin-exchange relaxation free (SERF) regime.

The π pulses also allow the magnetometer to sense a small transverse field due to nuclear spins in the presence of the larger B_0 field. This is illustrated in Fig. 20a), where the signal from a transverse field increases when rate of π pulses exceeds the rate of Rb spin precession in the B_0 field. The noise spectrum of the Rb magnetometer in a 1 cm diameter spherical cell is shown in Fig. 20b). The sensitivity of the magnetometer is equal to 40 fT/Hz $^{1/2}$ with a flat noise spectrum down to 1 Hz.

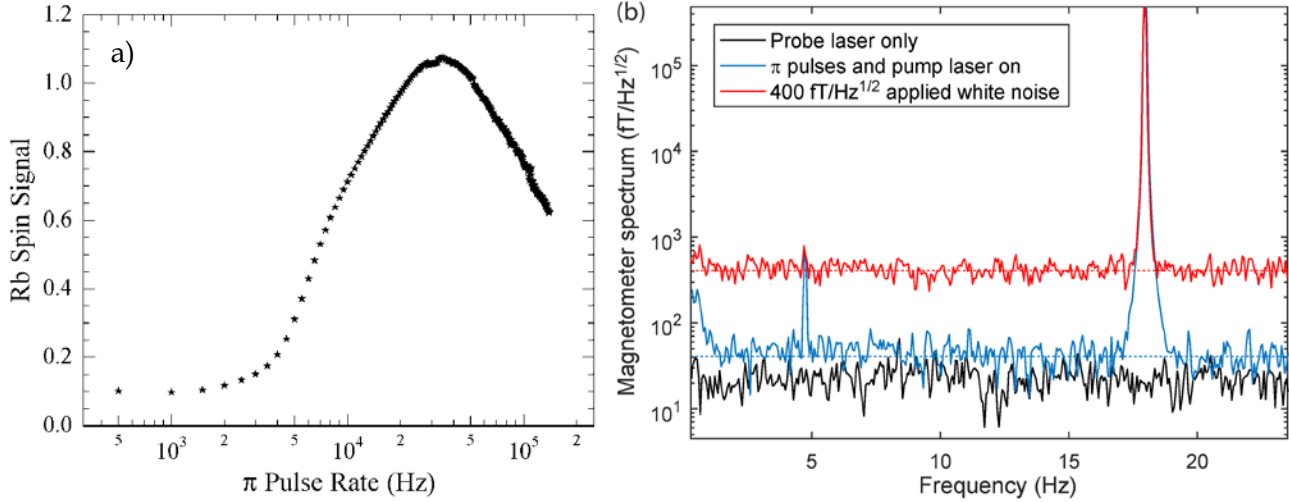


Fig. 20. Left panel: The Rb spin signal in response to a transverse magnetic field as a function of the π pulse rate; Right panel: Noise spectrum of the Rb magnetometer (green line) compared to the noise spectrum with an applied external white noise at 400 fT/Hz $^{1/2}$ (red line)

Operation of the magnetometer in anodically-bonded cells presents an additional challenge because they have only one optical access direction. For these cells we implemented a scheme using a pulsed probe laser, as illustrated in Fig. 21. The probe laser is parallel to the pump laser, but is only turned on for a short time during the π pulse. At the center of the π pulse the Rb spins are rotated by $\pi/2$ and the probe optical rotation signal crosses zero. The probe laser is turned on at that instance and can detect the initial rotation of the Rb spins away from the z axis due to the presence of a transverse magnetic field. The noise spectrum of the magnetometer signal in one of the anodically bonded cells is shown in Fig. 21b). The noise level is equal to about 300 fT/Hz $^{1/2}$, it roughly scales as the (cell volume) $^{1/2}$ compared to the larger spherical cell, as would be expected.

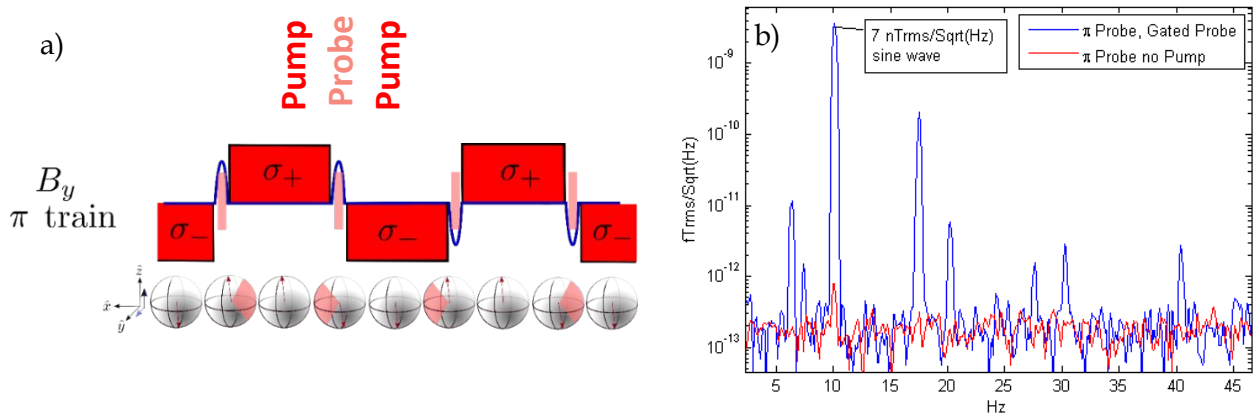


Fig. 21. a) Operation of the Rb magnetometer in anodically bonded cells with a single optical axis, the pump, probe and the bias magnetic fields are parallel to the optical axis of the cylinder and b) magnetometer noise spectrum in an anodically bonded cell

Operation of the magnetometer in a compact physics package presents an additional challenge in that the lasers cannot be easily modulated. For this configuration we developed a simple absorption magnetometer, where we monitor the transmission of circularly polarized light. The schematic of the magnetometer and the physics package are shown in Fig. 22. The package contains the lasers and the cell and maintains a physical size consistent with metrics of the C-SCAN program. This system is particularly simple to assemble and align.

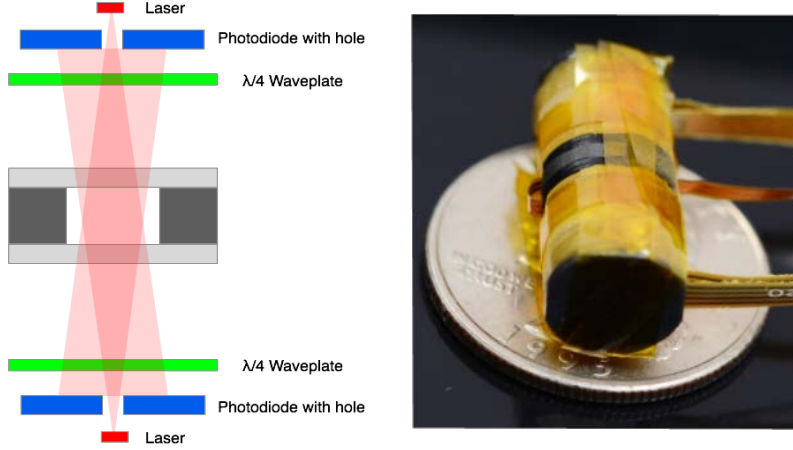


Fig. 22. Schematic and photo of the absorption mode magnetometer

The operation of the magnetometer is illustrated in Fig. 23a). We apply an additional modulation to the B_y field to intentionally misalign the Rb spin from the z axis by a small angle. The transmission through the cell is measured with a lock-in amplifier. A first harmonic signal at the modulation frequency is proportional to the presence of a transverse field in the y direction, such as caused by precessing nuclear spins. Fig. 23b) shows the magnetic field noise spectrum obtained with the transmission mode magnetometer with a sensitivity of about $200 \text{ fT/Hz}^{1/2}$ using Princeton Optronics VCSELs, similar to the sensitivity of the laboratory setup in the anodically-bonded cells.

The π pulses are applied as in the other schemes, while simultaneously detuning one of the VCSEL lasers off resonance and tuning the other one on resonance. Due to the thermal time constant of the VCSELs, the π pulse rate is only about 5 kHz, compared to 30 kHz in the laboratory system where an EOM is used to modulate the polarization of the light.

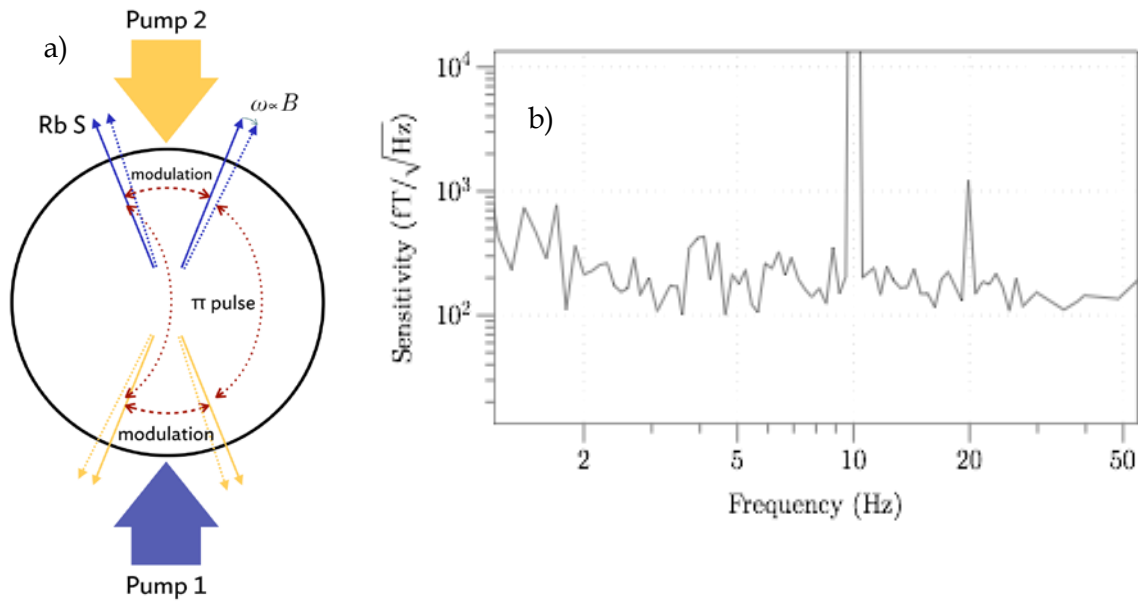


Fig. 23. Left panel: Schematic of the operation of absorption mode magnetometer; Right panel: Noise spectrum of the magnetometer using Princeton Optronics VCSEL

10.0 PERFORMANCE OF THE GYROSCOPE WITH SPHERICAL GLASS BLOWN CELLS.

We have explored the performance of the gyroscope in the three Rb magnetometer configurations: (1) with a glass-blown 10 mm diameter cell and orthogonal pump and probe beams derived from DFB lasers with AOM and EOM modulators, (2) with an anodically bonded 2 mm diameter cell and parallel pump and probe beams with external modulators, and (3) in the final physics package with a transmission magnetometer and current-modulated VCSEL lasers.

In the setup with glass-blown cells we used the free precession in-the-dark Ramsey technique. The timing sequence of the measurements is shown in Fig. 24a) and the Allan deviation plot is shown in Fig. 24b). The Allan deviation obtained in Phase 2 at 1 hour is equal to $0.025 \text{ deg}/\text{hour}^{1/2}$ and the bias drift is below $0.01 \text{ deg}/\text{hour}$. One can see an improvement in the sensitivity compared with the CW Zeeman RF depolarization scheme used in Phase 1.

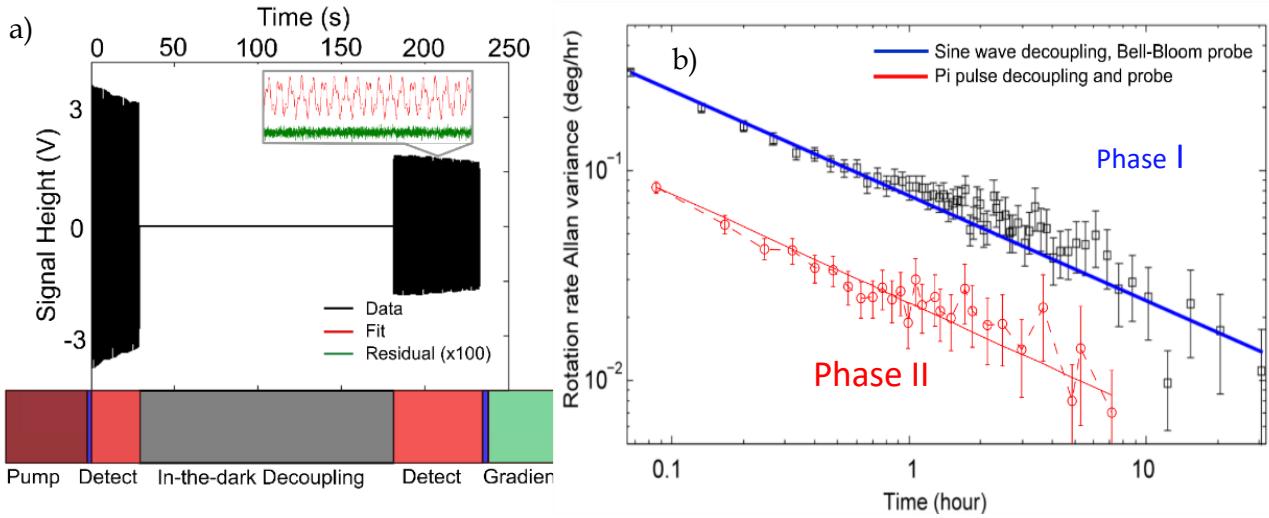


Fig. 24: a) Timing sequence of the gyroscope measurements, recorded signals, and fits to two spin precession frequencies and b) the Allan deviation plot obtained from a long run of repeated measurements comparing the performance in Phase 1 using CW RF repolarization and Phase 2 using π pulse sequences

The main effort in Phase 3 was to demonstrate the absolute accuracy of the gyroscope, i.e. absence of a bias offset. This required elimination of all systematic effects discussed in sections 5-7. To completely depolarize Rb atoms we used π pulses along both x and y direction. Using π pulses in the y plane does not completely eliminate the Rb polarization effect, but using π pulses in both x and y directions makes the frequency ratio largely independent of Xe amplitude and tip angle, as illustrated in Fig. 25a). Both planes of pulses are then rotated at the rotation frequency given by the intercepts indicated in Fig. 16. Careful attention was paid to eliminating metal conductors in the vicinity of the cells, to suppress the eddy current effects illustrated in Fig. 17. The pulses in x and y direction were generated by two separate circuits to eliminate their cross-talk, which can also look like a rotating pulse. To eliminate dipolar field effects the initial tipping pulse for nuclear spins was carefully calibrated. Reversing the He polarization allows one to optimize the pulse height so it has

no effect on the frequency ratio, as indicated in Fig. 25b). Any remaining transverse polarization at the end of the measurement was dephased using an applied gradient, so the next measurement starts from a well-defined state. These procedures are described in more detail in [5].

After all systematic effects are eliminated the frequency ratio is only affected by the projection of the Earth's rotation rate onto the direction of the bias field. The ratio of the gyromagnetic ratios, $\gamma_{\text{He}}/\gamma_{\text{Xe}}=2.7540813(3)$ is sufficiently well known [6] that we can measure the absolute rotation rate of the Earth without having to rotate the apparatus.

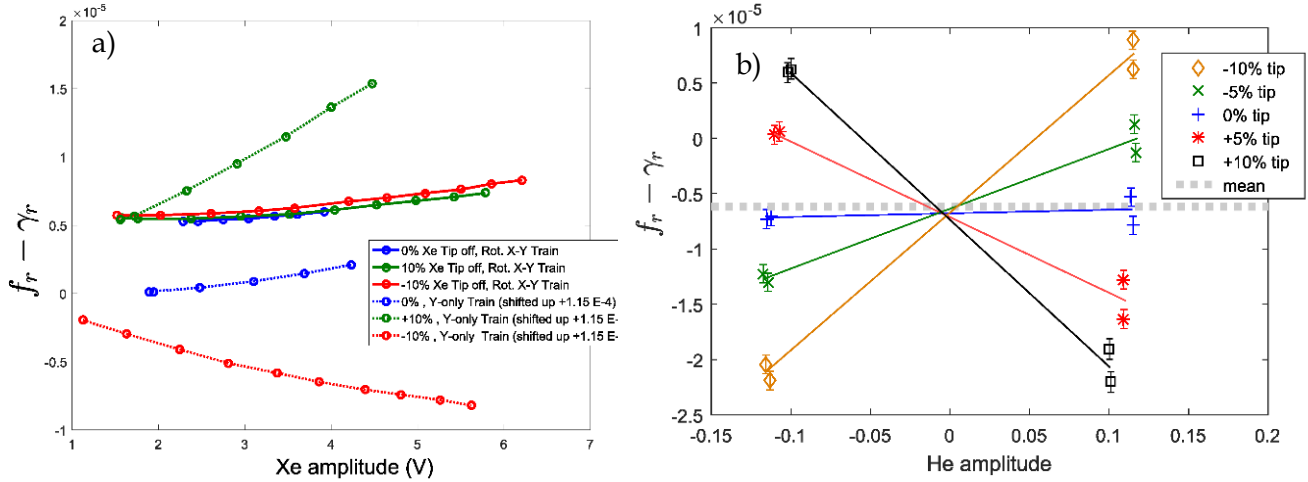


Fig. 25. a) Systematic shift in the frequency ratio due to Rb back-polarization by Xe and b) Systematic shift due to dipolar effects from He polarization if the initial 90 degree pulse is not perfect

In Fig. 26 we show the results of these measurements. We made measurements for 4 possible orientations of the B_0 field in the horizontal plane, without changing the mechanical orientation of the apparatus, as illustrated in Fig. 26a). From the knowledge of the building orientation we can calculate the expected projection of the Earth's rotation rate on the bias field direction. Fig. 26b) shows the comparison of the expected signals (solid lines) to the averaged measured signals (dashed lines). Fig. 26c) shows the dependence of the frequency ratio on the bias magnetic field, indicating that it follows the expected behavior without any free parameters. The measurements generally agree with prediction. The average value of the discrepancy (dominated by one point) is equal to 2.5 deg/hour and the worst discrepancy is 5 deg/hour. This corresponds to the size of an absolute bias offset, without any calibrations. In many inertial rotation sensing methods the bias offset depends on the mechanical properties of the system and needs to be individually modelled. In contrast, nuclear spin gyroscopes do not have an intrinsic unknown bias offset as long as systematic effects are well controlled.

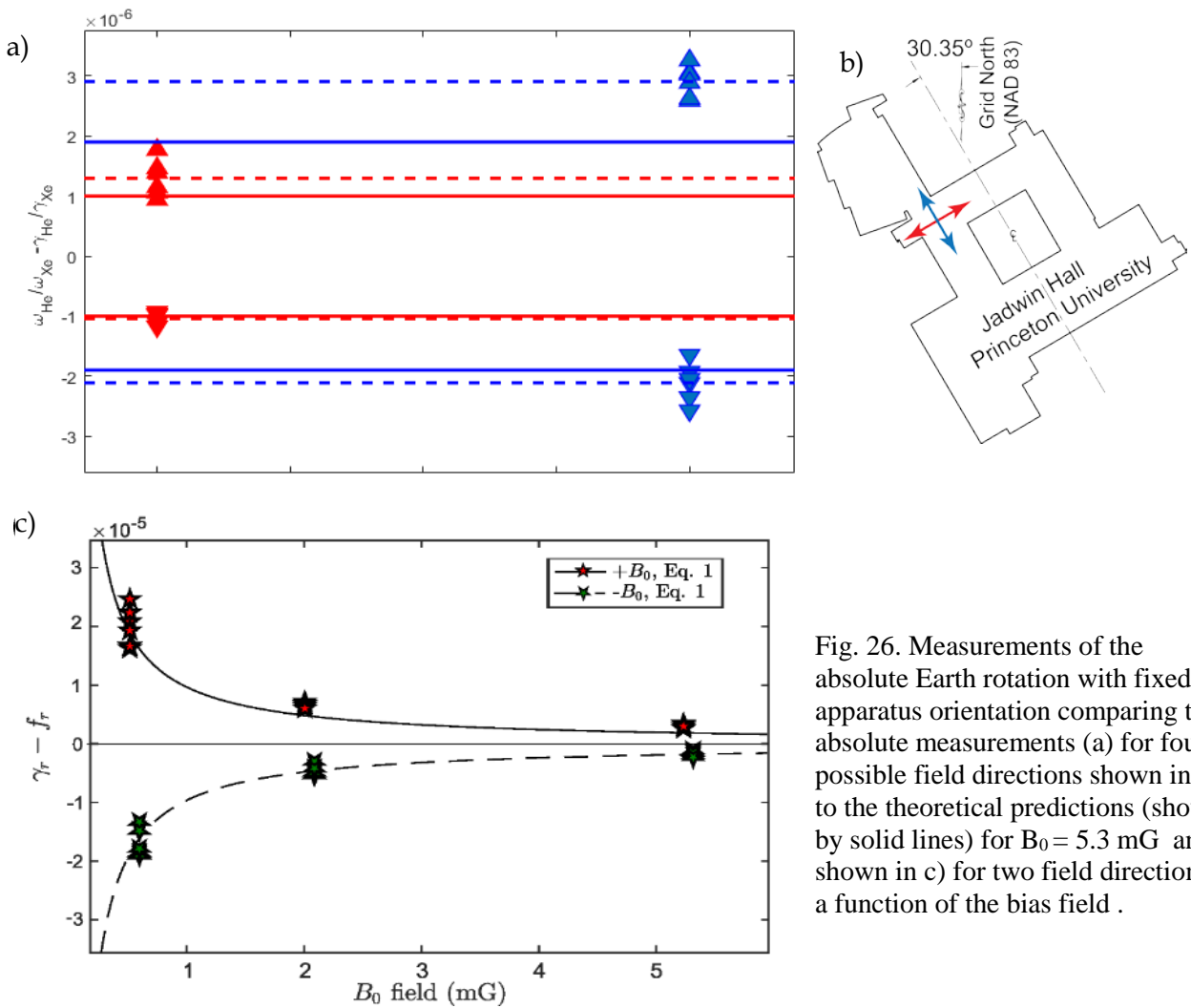


Fig. 26. Measurements of the absolute Earth rotation with fixed apparatus orientation comparing the absolute measurements (a) for four possible field directions shown in (b) to the theoretical predictions (shown by solid lines) for $B_0 = 5.3$ mG and shown in c) for two field directions as a function of the bias field .

11.0 PERFORMANCE OF THE GYROSCOPE WITH ANODICALLY BONDED CELLS.

We investigated the performance of 2 mm. diameter anodically bonded cells using the laboratory setup with co-linear pump and probe lasers. The power of the laser beams used in the measurements was on the order of 0.5 mW but they were modulated using external AOM and EOM devices. In Fig. 27 we show the performance of the gyroscope using either precession in the dark technique or a continuous measurement while only applying y axis π pulses. The angle random walk (ARW) is equal to 1 deg/hour^{1/2} for the in-the-dark measurement technique and 0.4 deg/hour^{1/2} for the continuous measurement technique. The bias drift was \leq 0.2 deg/hour. The uncertainty in both cases is limited by the frequency resolution of the ³He precession signals. Increasing the ³He pressure from 2 atm. to 5-10 atm. as in the glass-blown cells would significantly improve the performance. We also investigated the absolute bias offset in the anodically bonded cells and found it to be similar to the bias offset in the spherical glass blown cells.

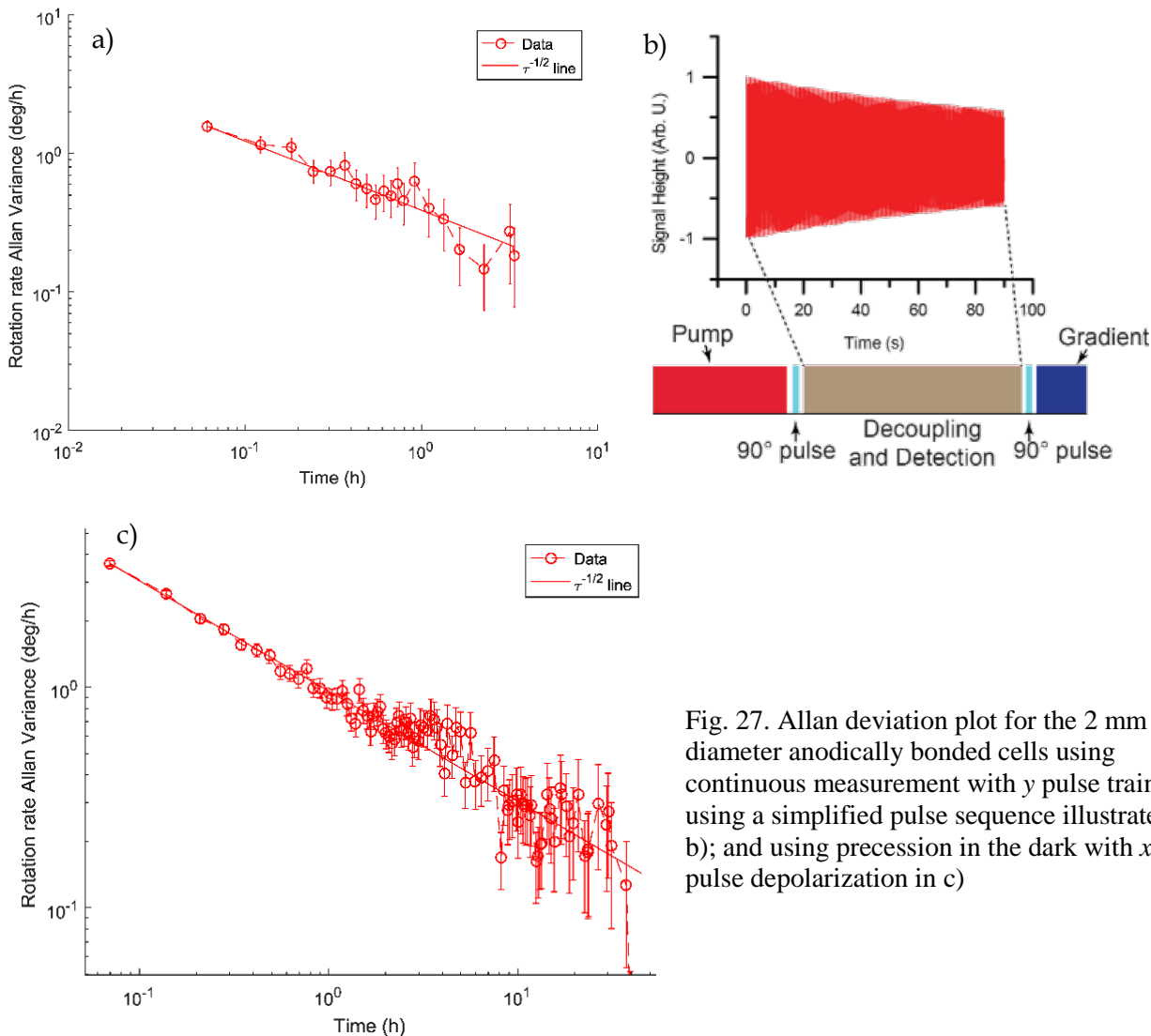


Fig. 27. Allan deviation plot for the 2 mm diameter anodically bonded cells using continuous measurement with y pulse train a), using a simplified pulse sequence illustrated in b); and using precession in the dark with x-y pulse depolarization in c)

12.0 PERFORMANCE OF THE GYROSCOPE IN THE PHYSICS PACKAGE.

The physics package using the absorption mode magnetometer allowed easy exchange of the VCSEL modules used for optical pumping and detection. Sensors with several different 795 nm VCSEL lasers from Princeton Optronics and from Vixar were investigated. The Princeton Optronics lasers provided up to 1 mW of light at 3 mA and showed good magnetometer sensitivity as shown in Figure 23, but did not have a stable polarization or frequency mode, which made them unusable for long term measurements. The Vixar 795S series provided less power, about 150 μ W with 2 mA of current, but the output had a stable single wavelength mode and a stable polarization state thanks to an internal polarization grating.

The VCSELs were current modulated on and off the absorption resonance synchronously with the π pulses applied to the Rb spins to ensure the atoms were pumped with circularly polarized light in both forward and reverse orientations. The current modulation and the emitter's thermal response generate a non-stationary laser wavelength that was generally centered on the absorption resonance but was changing throughout the period, resulting in less efficient optical pumping. Frequency noise from a VCSEL can be suppressed if it is tuned exactly to the absorption peak where small changes in laser frequency change the transmission only in second order. However, the laser frequency noise was poorly suppressed due to unavoidable laser wavelength variation during the modulation.

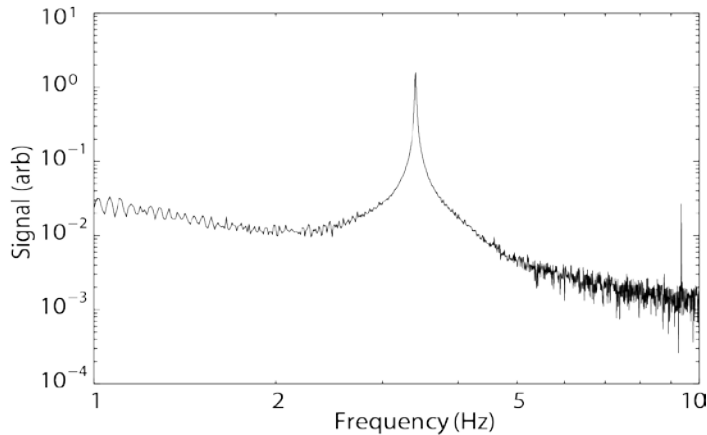


Figure 28. Spectrum of typical gyroscope signal showing ^{129}Xe and ^3He peaks in the physics package.

In the compact sensor, the ^3He T_2 was found to be about 1 hour. The helium relaxation is consistent with a gradient imposed by the laser current running in a ~2 mm loop about 7 mm from the cell. The cell stack was lengthened using spacers, but the ^3He lifetime did not improve so we conclude gradients are generated from additional sources such as the flexible circuit board leads. The ^{129}Xe T_2 was typically 35 seconds at the operating temperature. Significantly longer Xe T_2 is observed at lower temperature; however, the cell was heated to obtain a higher temperature to increase the ^3He signal. The spectrum of typical gyroscope signals is shown in Fig. 28. Note a significant 1/f component of the noise background, due to wavelength instability of modulated VCSEL lasers. The uncertainty of the ^{129}Xe frequency for a typical precession cycle was ± 2 ppm whereas for ^3He

it was ± 30 ppm. We find a clear need to further increase ^3He signal through increased ^3He pressure or by reducing the field gradients and increasing the optical pumping power.

A stand-alone control system was developed to control all parts of the gyroscope operation. The integrated control unit included a cell heater controller, two laser controllers, a three-channel current supply for magnetic field compensation, a three-channel pulse driver for applying π pulses, and two photodiode amplifiers connected to two high performance 24-bit ADCs. A high performance microcontroller coordinates all aspects of the system and performs lock-in demodulation of all signals. The entire gyroscope system is controlled over and powered from a USB port. Fig. 29 shows a picture of the control electronics.

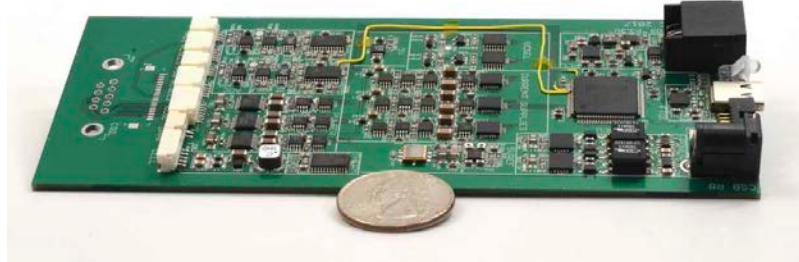


Figure 29. Integrated control electronics for entire gyroscope operation powered from a USB port.

The gyroscope was operated in a laboratory magnetic shield and coil system using the physics package containing the lasers, heaters, VCSELs and photodiodes, as illustrated in Fig. 22. Fig. 30 shows the angular rotation data from the gyroscope and the Allan deviation using a Vixar VCSEL. We achieved an ARW of $8 \text{ deg/hour}^{1/2}$, limited by the ^3He signal amplitude, and a bias drift on the order of 3 deg/hour . Princeton Optronics VCSELs provided higher ^3He signals, but multiple attempts of long term operation after careful emitter selection and polarization compensation did not provide a sensor with good long term performance.

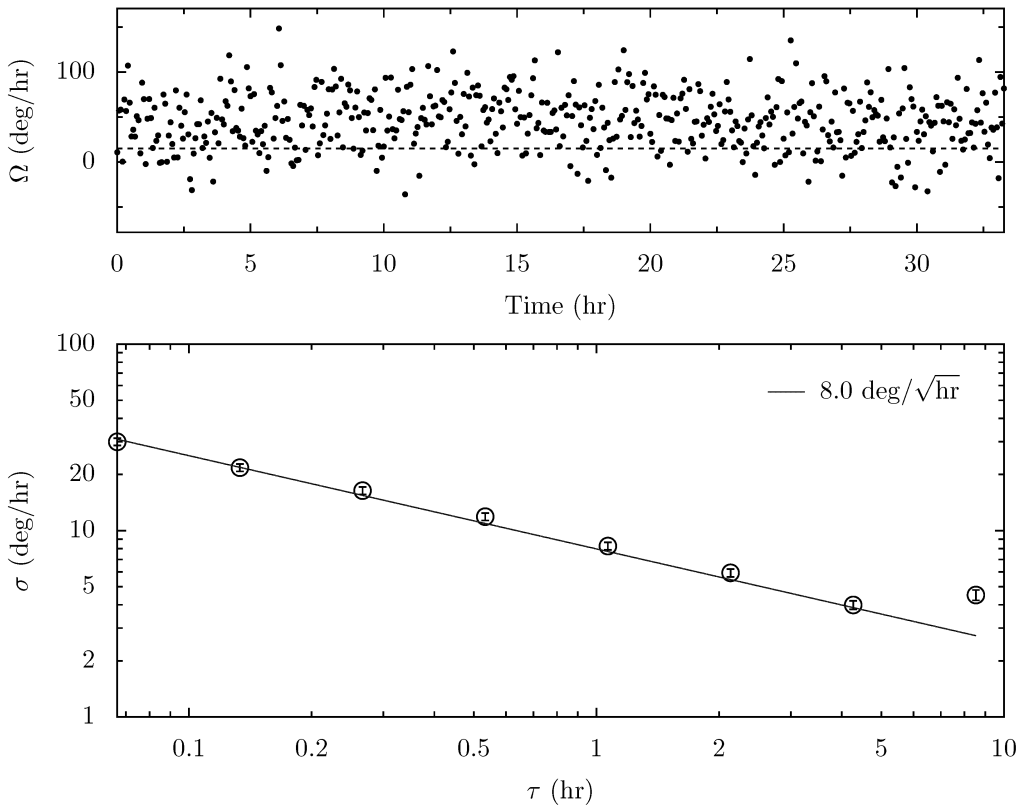


Figure 30. Gyroscope performance in the physics package.

13.0 ESTIMATES OF FUNDAMENTAL GYROSCOPE SENSITIVITY.

We can estimate the fundamental limits of the gyroscope sensitivity by analyzing the signal-to-noise ratio (SNR) of the recorded signals. Fig. 31 shows the time domain and the frequency spectrum of a typical gyroscope signal acquired with the spherical glass-blown cell. The two largest peaks correspond to ^{129}Xe and ^3He signals, the others are cross-modulation peaks due to non-linearity of the Rb magnetometer response. The frequency spectrum shows extremely high SNR of the nuclear spin precession signals. For ^{129}Xe the initial $\text{SNR} = 5\text{V}/(1.5 \times 10^{-5} \text{ V/Hz}^{1/2}) = 3 \times 10^5 \text{ Hz}^{1/2}$.

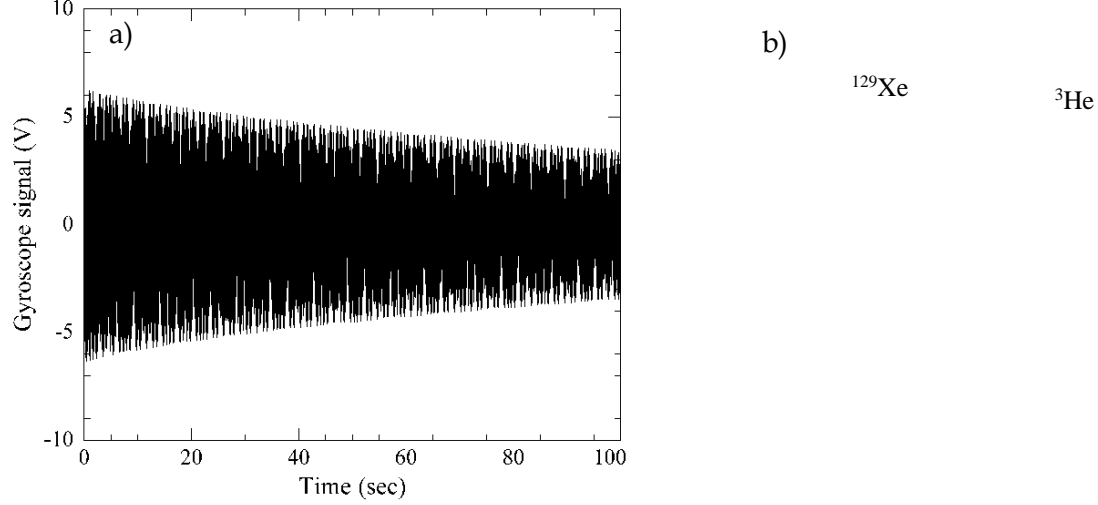


Fig. 31. a) Time domain and b) frequency spectrum of the gyroscope signal, the red line shows the Rb magnetometer noise spectrum in the absence of nuclear spin signals.

The frequency uncertainty for fitting a decaying sine wave to the signal over a time interval τ is given by the Cramer-Rao limit

$$\delta\omega = \frac{\sqrt{12} C(\tau/T_2)}{\text{SNR } \tau^{3/2}}, \quad (11)$$

where $C(\tau/T_2)$ is a function that quantifies the loss in sensitivity due to decay of the signal, for the signal in Fig. 31a), $C(\tau/T_2)=1.5$ [7]. We find an ideal frequency uncertainty of $\delta\omega_{\text{Xe}}=1.4 \times 10^{-8} \text{ rad/s}$ after each measurement cycle. The total measurement cycle time is about 130 sec, so the expected ARW=0.001 deg/hour $^{1/2}$. In practice our ARW is significantly worse. When optimizing for best short-term sensitivity we experimentally obtained ARW=0.01 deg/hour $^{1/2}$.

Part of the reason for reduction in short term sensitivity is the presence of many cross-modulation peaks seen in Fig. 31b). These peaks appear at frequencies $\omega_{\text{He}}-2\omega_{\text{Xe}}$, $3\omega_{\text{Xe}}$ and other combinations, due to the 3rd order nonlinearity in the response of the Rb magnetometer. The size of these peaks can be reduced by fitting the data to a more complicated lineshape. However, we have not been able to completely eliminate the cross-modulation peaks. As a result, the fitting error is significantly worse than predicted by the Cramer-Rao limit. This limitation will need to be investigated more in the future.

14.0 DEVELOPMENT OF COMPACT FERRITE SHIELD-COIL SYSTEM.

The initial design of the physics package included a compact system of coils and shields. The design goal is an axial field with 1:1000 field uniformity throughout the 2 mm cell volume. For reference, a lower uniformity of 1:100 would limit the ^3He T₁ to about 15 minutes. We were able to simulate a 1 cm diameter coil that meets these specification. However, fabricating such a coil using standard flexible kapton circuit board, shown in Fig. 32a) leads to uniformity far less than the design values due to limitations on the dimensional tolerances of flexible circuits. To avoid the fabrication tolerance problems we evaluated the use of a ferrite magnetic shield with coils that penetrate the shield material. Ferrite with penetrating coils has the potential to be fabricated with much tighter mechanical tolerances using precision machining and rigid wires. However, the tolerance on magnetic permeability limits the ability to achieve ideal and reproducible results. While 2D simulations were promising, a fully 3D simulation revealed that one axis always has a significant gradient. These findings were supported by experimental measurements shown in Fig. 32b) with a shield-coil prototype. Additional coils may be able to compensate for the field gradient. However, we did not pursue this part of the project further and did not incorporate small coils and shields into our physics package.

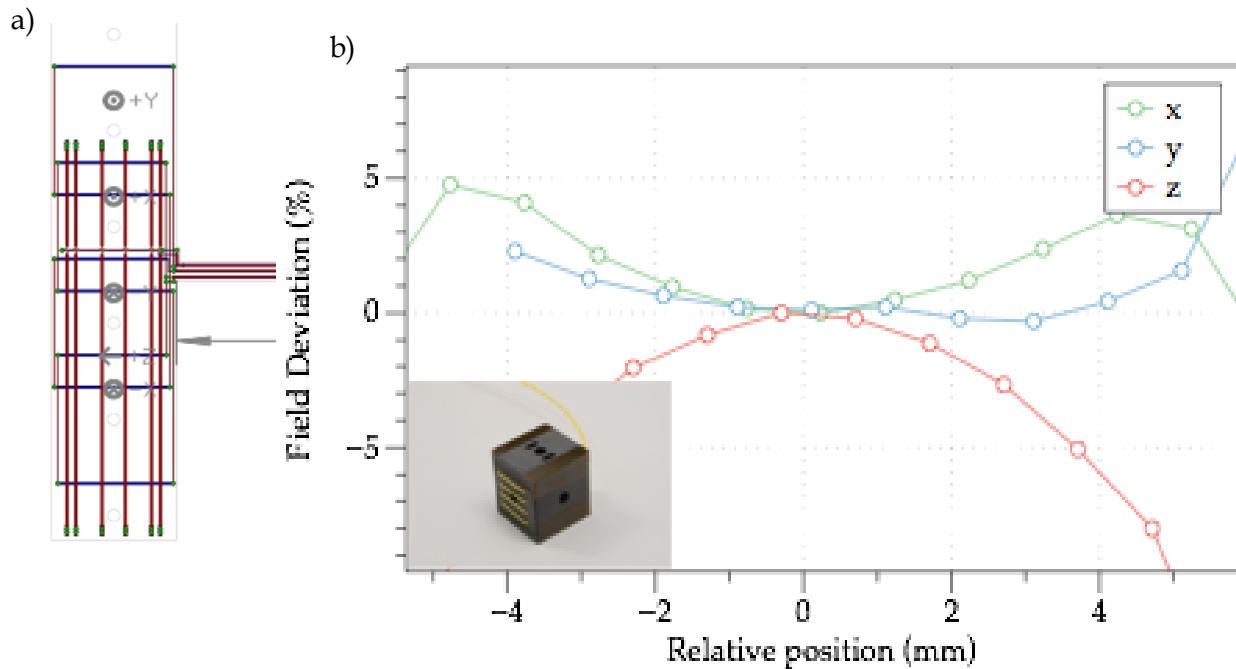


Fig. 32:Cylindrically-wrapped field coil made from a kapton circuit a) for use in a cylindrical shield and measurements of the magnetic field inside a ferrite shield b) with penetrating wires (inset) using a GMR sensor.

15.0 DISCUSSION AND CONCLUSIONS.

During this project we developed a number of techniques to advance the state of the art in nuclear spin gyroscopes. We fabricated anodically bonded batch-fabricated cells with excellent spin-relaxation processes. We developed several methods for measurement of the gyroscope signals with a high SNR. We explored a number of systematic effects that can limit the long term bias stability of nuclear spin gyroscopes and developed methods to suppress them.

Our results also indicate a number of limitations that will need to be overcome. For fabrication of anodically bonded cells it will be important to increase the pressure of the ${}^3\text{He}$ buffer gas. This will increase the size of ${}^3\text{He}$ signals, which presently limit sensitivity in the small cells. It will also reduce the spin relaxation of Rb atoms by limiting diffusion to cell walls, allowing us to use lower power Vixar VCSEL lasers. The ${}^3\text{He}$ pressure can be increased by upgrading the mechanical structure of the anodic bonding system to withstand gas pressure up to 10 atm.

It will be interesting to explore incorporation of a light modulator into the physics package design. Direct current modulation of VCSEL lasers is relatively slow and, more importantly, causes a great deal of frequency instability even when dealing with fairly broad optical absorption lines in a buffer gas cell. One can imagine using a miniature and fast MEMS intensity modulator that can operate at 10-30 kHz, for example a resonant piezo structure. Another possibility is to use an integrated LiNbO_3 polarization modulator. Using a modulator will allow us to leave the VCSELs at a constant current, increasing their stability and simplifying frequency locking.

Based on Allan deviation of repeated measurements we obtained an $\text{ARW} = 0.025 \text{ deg/hour}^{1/2}$ for a 10 mm diameter cell and $\text{ARW} = 0.4 \text{ deg/hour}^{1/2}$ in anodically-bonded 2 mm diameter cell. Comparing these results to the Cramer-Rao limit for the recorded signals we find that a significant improvement in ARW is possible by better modelling the shape of the signal to eliminate the cross-modulation peaks introduced by the non-linearity of the Rb magnetometer. Based on SNR of recorded signals an $\text{ARW} = 0.01 \text{ deg/hour}^{1/2}$ is quite feasible in a 2 mm diameter cell with optimized ${}^3\text{He}$ pressure.

We established that our approach has an inherently small bias offset and good long term stability. No obvious effects of bias drift were observed on a time scales of 10 hours and bias stability of better than 0.01 deg/hour was demonstrated. We are able to measure the bias offset due to Earth rotation without any offset calibration or mechanical rotation of the gyroscope.

The results of this research have been published in [2,3], one paper under review [5], and one paper on anodically bonded cells being prepared for publication.

16. REFERENCES

- [1] G. D. Cates, S. R. Schaefer, and W. Happer, *Relaxation of spins due to field inhomogeneities in gaseous samples at low magnetic fields and low pressures*, Phys. Rev. A **37**, 2877 (1988).
- [2] D. Sheng, A. Kabcenell, and M. V. Romalis, *New Classes of Systematic Effects in Gas Spin Comagnetometers*, Phys. Rev. Lett. **113**, 163002 (2014).
- [3] N. Dural and M.V. Romalis, *Gallium phosphide as a new material for anodically bonded atomic sensors*, APL Materials **2**, 086101 (2014).
- [4] M. Bulatowicz, R. Griffith, M. Larsen, J. Mirjianian, C. B. Fu, E. Smith, W. M. Snow, H. Yan, and T. G. Walker, *Laboratory Search for a Long-Range T-Odd, P-Odd Interaction from Axionlike Particles Using Dual-Species Nuclear Magnetic Resonance with Polarized ^{129}Xe and ^{131}Xe Gas*, Phys. Rev. Lett. **111**, 102001 (2013).
- [5] M. E. Limes, D. Sheng, and M. V. Romalis, *^3He - ^{129}Xe Co-magnetometry using ^{87}Rb Detection and Decoupling*, arXiv:1708.05772
- [6] W. Makulski, *^{129}Xe and ^{131}Xe nuclear magnetic dipole moments from gas phase NMR spectra*, Magnetic Resonance in Chemistry **53**, 273 (2015),
- [7] C. Gemmel, W. Heil, S. Karpuk, K. Lenz, Ch. Ludwig, Yu. Sobolev, K. Tullney, M. Burghoff, W. Kilian, S. Knappe-Grüneberg, W. Müller, A. Schnabel, F. Seifert, L. Trahms, and St. Baeßler, *Ultra-sensitive magnetometry based on free precession of nuclear spins*, Eur. Phys. J. D **57**, 303 (2010).

LIST OF SYMBOLS, ABBREVIATIONS, AND ACRONYMS

ADC	Analog to Digital Converter
AOM	Acousto optic Modulator
ARW	Angle Random Walk
CMOS	Complementary metal oxide semiconductor
CW	Continuous Wave
DFB	Distributed Feedback laser
EOM	Electro optic Modulator
GMR	Giant magnetoresistance
PID	Proportional Integral Feedback
RF	Radio Frequency
SERF	Spin Exchange Relaxation Free
SNR	Signal to Noise Ratio
TEC	Thermo Electric Cooler
USB	Universal Serial Bus
VCSEL	Vertical Cavity Surface Emitting Laser
ω	Precession frequency
γ	Gyromagnetic ratio
T	Temperature
B	Magnetic field
D	Diffusion constant
f_r	Frequency ratio
γ_r	Ratio of gyromagnetic ratios
τ	Measurement time
T_2	Transverse spin relaxation time
P	Polarization